



ELSEVIER

Fluid Dynamics Research 33 (2003) 509–544

---

---

**FLUID DYNAMICS  
RESEARCH**

---

---

# Gross–Pitaevskii dynamics of Bose–Einstein condensates and superfluid turbulence

M. Abid<sup>a</sup>, C. Huepe<sup>b</sup>, S. Metens<sup>c</sup>, C. Nore<sup>d</sup>, C.T. Pham<sup>e</sup>, L.S. Tuckerman<sup>d</sup>,  
M.E. Brachet<sup>e,\*</sup>

<sup>a</sup>*Institut de Recherche sur les Phénomènes Hors Equilibre, U M R 6594 associé au CNRS et aux Universités d'Aix-Marseille I et II, 49 rue Joliot Curie, Marseille 13384, France*

<sup>b</sup>*James Franck Institute, University of Chicago, 5640 S. Ellis Ave., Chicago, IL 60637, USA*

<sup>c</sup>*Laboratoire de Physique Théorique de la Matière Condensée, Université Paris VII, 75005 Paris, France*

<sup>d</sup>*Laboratoire d'Informatique pour la Mécanique et les Sciences de l'Ingénieur, BP133, Orsay 91403, France*

<sup>e</sup>*Laboratoire de Physique Statistique de l'Ecole Normale Supérieure, associé au CNRS et aux Universités Paris VI et VII, 24 Rue Lhomond, Paris 75231, France*

Received 9 December 2002; received in revised form 5 September 2003; accepted 5 September 2003

Communicated by S. Kida

---

## Abstract

The Gross–Pitaevskii equation, also called the nonlinear Schrödinger equation (NLSE), describes the dynamics of low-temperature superflows and Bose–Einstein Condensates (BEC). We review some of our recent NLSE-based numerical studies of superfluid turbulence and BEC stability. The relations with experiments are discussed.

© 2003 Published by The Japan Society of Fluid Mechanics and Elsevier B.V. All rights reserved.

*Keywords:* Superfluid turbulence; Bose–Einstein condensates; Gross–Pitaevskii equation; Bifurcation and dynamics; Exact results; Branch following method

---

## 1. Introduction

The present paper is a review of results, obtained by our group during the last 10 years, by numerically studying the nonlinear Schrödinger equation (NLSE). Direct numerical simulations (DNS) and branch-following methods were extensively used to investigate the dynamics and stability of NLSE solutions in 2 and 3 space dimensions.

---

\* Corresponding author.

*E-mail address:* [marc-etienne.brachet@lps.ens.fr](mailto:marc-etienne.brachet@lps.ens.fr) (M.E. Brachet).

Much work has been devoted to the determination of the critical velocity at which superfluidity breaks into a turbulent regime (Donnelly, 1991). A mathematical model of superfluid  $^4\text{He}$ , valid at temperatures low enough for the normal fluid to be negligible, is the nonlinear Schrödinger equation (NLSE), also called the Gross–Pitaevskii equation (Gross, 1961; Pitaevskii, 1961; Landau and Lifchitz, 1980). In a related context, dilute Bose–Einstein condensates (BEC) have been recently produced experimentally (Anderson et al., 1995; Davis et al., 1995; Bradley et al., 1997). The dynamics of these compressible nonlinear quantum fluids is accurately described by the NLSE allowing direct quantitative comparison between theory and experiment (Dalfovo et al., 1999).

Excitations of superfluid  $^4\text{He}$  are described by the famous Landau spectrum which includes phonons in the low wave number range, and maxons and rotons in the high (atomic-scale) wave number range. In contrast, the standard NLSE (the equation used in the present paper) contains only phonon excitations. It therefore incompletely represents the atomic-scale excitations in superfluid  $^4\text{He}$ . However, note that there exist generalizations of the NLSE (Pomeau and Rica, 1993; Roberts and Berloff, 2001) that do reproduce the correct excitation spectrum, at the cost of introducing a spatially nonlocal interaction potential.

Several problems pertaining to superfluidity and BEC can thus be studied in the framework of the NLSE. In this review, we concentrate on two such problems: (i) low-temperature superfluid turbulence (Nore et al., 1997a, b; Abid et al., 1998) and (ii) stability of BEC in the presence of a moving obstacle (Huepe and Brachet, 1997, 2000; Nore et al., 2000) or an attractive interaction (Huepe et al., 1999, 2003).

The authors recognize that this paper relates for the most part to their own work and does not include important and relevant contributions by other authors. However, we now give a short (and partial) list of references to provide a starting point to the reader motivated to undertake a deeper exploration of the field. A recent review of superfluid turbulence can be found in Vinen and Niemela (2002) and a proceeding devoted to the same subject is the paper by Barenghi et al. (2001). Alternate simulations (by Biot–Savart vortex methods) of low-temperature superfluid turbulence can be found in Araki et al. (2002). Reconnection and acoustic emission are studied in Ogawa et al. (2002). A standard reference on the subject of vortex reconnection is the article by Koplik and Levine (1993). Cascade processes and Kelvin waves are investigated in Araki and Tsubota (2000), Leadbeater et al. (2003), Kivotides et al. (2001), Svistunov (1995) and Vinen (2001). Recent (very) low-temperature experiments in Helium are described in Davis et al. (2000). The experimental field of Bose–Einstein condensation is in rapid evolution. Recent results include the observation of an isolated quantum vortex (Matthews et al., 1999; Inouye et al., 2001) and the nucleation of several vortices (Madison et al., 2000). Details of vortex dynamics (Rosenbush et al., 2002) and even Kelvin waves (Bretin et al., 2003) are now being observed.

The present paper is organized as follows: in Section 2 the basic definitions and properties of the model of superflow are given. A short presentation of the hydrodynamic form, through Madelung’s transformation, of NLSE with an arbitrary nonlinearity is derived. Simple solutions are discussed.

Section 3 is devoted to superfluid turbulence. The basic tools that are needed to numerically study 3D turbulence using NLSE are developed and validated in Section 3.1. The NLSE numerical results are given in Section 3.2. Experimental results are given in Section 3.3.

The stability of BEC is studied in Section 4. Exact 1D results are given in Section 4.1 and a general formulation of stability is given in Section 4.2. Numerical branch-following methods are explained in Section 4.3. The stability of a superflow around a cylinder is studied in Section 4.4.

The stability of an attractive Bose–Einstein condensate is studied in Section 4.5. Finally, Section 5 is our conclusion.

## 2. Hydrodynamics using the NLSE

The hydrodynamical form of NLSE with an arbitrary nonlinearity, corresponding to a barotropic fluid with an arbitrary equation of state, is introduced in this section. Basic hydrodynamic features such as acoustic propagation and stationary vortex solutions are also discussed.

### 2.1. Madelung’s transformation

The connection between the NLSE and fluid dynamics can be obtained directly using the following action (Spiegel, 1980):

$$\mathcal{A} = 2\alpha \int dt \left\{ \int d^3x \left( \frac{i}{2} \left( \bar{\psi} \frac{\partial \psi}{\partial t} - \psi \frac{\partial \bar{\psi}}{\partial t} \right) \right) - \mathcal{F} \right\} \quad (1)$$

with

$$\mathcal{F} = \int d^3x (\alpha |\nabla \psi|^2 + f(|\psi|^2)), \quad (2)$$

where  $\psi(\vec{x}, t)$  is a complex wave field and  $\bar{\psi}$  its complex conjugate,  $\alpha$  is a positive real constant and  $f$  is a polynomial in  $|\psi|^2 \equiv \bar{\psi}\psi$  with real coefficients:

$$f(|\psi|^2) = -\Omega |\psi|^2 + \frac{\beta}{2} |\psi|^4 + f_3 |\psi|^6 + \dots + f_n |\psi|^{2n}. \quad (3)$$

The NLSE is the Euler–Lagrange equation of motion for  $\psi$  corresponding to (1). It reads

$$\frac{\partial \psi}{\partial t} = -i \frac{\delta \mathcal{F}}{\delta \bar{\psi}}$$

or

$$\frac{\partial \psi}{\partial t} = i(\alpha \nabla^2 \psi - \psi f'(|\psi|^2)). \quad (4)$$

Madelung’s transformation (Spiegel, 1980; Donnelly, 1991)

$$\psi = \sqrt{\rho} \exp\left(i \frac{\varphi}{2\alpha}\right) \quad (5)$$

maps the nonlinear wave dynamics of  $\psi$  into equations of motion for a fluid of density  $\rho$  and velocity  $\mathbf{v} = \nabla \varphi$ . Indeed, using (5), Eq. (1) can be written as

$$\mathcal{A} = - \int dt d^3x \left( \rho \frac{\partial \varphi}{\partial t} + \frac{1}{2} \rho (\nabla \varphi)^2 + 2\alpha f(\rho) + \frac{1}{2} (2\alpha \nabla(\sqrt{\rho}))^2 \right) \quad (6)$$

and the corresponding Euler–Lagrange equations of motion become

$$\frac{\partial \rho}{\partial t} + \nabla \cdot (\rho \mathbf{v}) = 0, \quad (7)$$

$$\frac{\partial \varphi}{\partial t} + \frac{1}{2} (\nabla \varphi)^2 + 2\alpha f'(\rho) - 2\alpha^2 \frac{\Delta \sqrt{\rho}}{\sqrt{\rho}} = 0. \quad (8)$$

These equations are the continuity and Bernoulli equation (Landau and Lifchitz, 1980) for an isentropic, compressible and irrotational fluid if one drops the last term of (8). This term is called the “quantum pressure”.

Using this identification, one can define the following “thermodynamic functions”.<sup>1</sup> First, by inspecting the Bernoulli equation, the fluid’s enthalpy per unit mass is given by

$$h = 2\alpha f'(\rho). \quad (9)$$

Second, noting that  $\frac{1}{2} \rho (\nabla \varphi)^2$  corresponds to kinetic energy in Eq. (6), the fluid’s internal energy per unit mass reads

$$e = \frac{2\alpha f(\rho)}{\rho}. \quad (10)$$

The general thermodynamic relation

$$h = e + p/\rho, \quad (11)$$

gives the expression

$$p = 2\alpha(\rho f'(\rho) - f(\rho)) \quad (12)$$

for the fluid’s pressure.

The units of the variables used in (2) and (3) can be recovered as follows: Madelung’s transformation (5) leads to  $[|\psi|^2] = [\rho] = ML^{-3}$  and  $[\alpha] = L^2 T^{-1}$ . Using (10), one gets  $[f(\rho)/\rho] = T^{-1}$  and thus, from (3),  $[\Omega] = T^{-1}$ ,  $[\beta] = T^{-1} \rho^{-1}$  and  $[f_i] = T^{-1} \rho^{1-i}$ . Note that, in the case of a Bose condensate of particles of mass  $m$ ,  $\alpha$  has the value  $\hbar/2m$  (Nozières and Pines, 1990).

## 2.2. Sound waves

### 2.2.1. Dispersion relation

The effect of the quantum pressure term in (8) can be found, at least to linear order, by means of the dispersion relation of acoustic (density) waves propagating in a constant density background  $\rho_0$ . Writing  $\rho = \rho_0 + \delta\rho$  (with  $f'(\rho_0) = 0$ ),  $\nabla \varphi = \delta\mathbf{v}$  in (7) and in the gradient of (8), one obtains (keeping only the linear terms)

$$\partial_t \delta\rho + \rho_0 \nabla \delta\mathbf{v} = 0,$$

$$\partial_t \delta\mathbf{v} + 2\alpha f''(\rho_0) \nabla \delta\rho - 2\alpha^2 \Delta \frac{\nabla \delta\rho}{2\rho_0} = 0$$

<sup>1</sup> Being isentropic ( $S = 0$ ), the fluid is barotropic, and only one independent thermodynamic variable is needed.

or

$$\partial_t^2 \delta\rho = 2\alpha\rho_0 f''(\rho_0)\Delta\delta\rho - \alpha^2 \Delta^2 \delta\rho.$$

The dispersion relation for an acoustic wave  $\delta\rho = \varepsilon(\exp(i(\omega t - \mathbf{k} \cdot \mathbf{x})) + \text{c.c.})$  (with  $\varepsilon \ll 1$ ) is thus

$$\omega = \sqrt{2\alpha\rho_0 f''(\rho_0)k^2 + \alpha^2 k^4}, \tag{13}$$

where  $k = |\mathbf{k}|$ . It is clear from this relation that the quantum pressure has a noticeable dispersive effect for large wave numbers. For small wave numbers, the usual propagation, with a constant speed of sound given by

$$c = \left(\frac{\partial p}{\partial \rho}\right)^{1/2} = \sqrt{2\alpha\rho_0 f''(\rho_0)},$$

is recovered. The length scale  $\xi = \sqrt{\alpha/(\rho_0 f''(\rho_0))}$  at which dispersion becomes noticeable is known as the coherence length.

### 2.2.2. Nonlinear acoustics

The description given by linear acoustics can be somewhat improved by including the dominant nonlinear effects. Such an equation was derived in Nore et al. (1993).

Numerical simulations of NLSE in one space dimension using a standard Fourier pseudo-spectral method (Gottlieb and Orszag, 1977) can be used to study the acoustic regime triggered by an initial disturbance of the form

$$\psi(x) = 1 + ae^{-x^2/l^2}.$$

Such simulations were performed in Nore et al. (1993) where it was found that the shocks which would have appeared under compressible Euler dynamics (i.e. following (8) without the last term in l.h.s.) are regularized by the dispersion. There was no evidence of finite-time singularity in our numerics: the spectrum of the solution was well resolved, with a conspicuous exponential tail.

### 2.3. Vortices in 2D and 3D

Stationary solutions of the equations of motion can give more insight into the connection between the NLSE and fluid dynamics. Indeed, stationary solutions of NLSE (4) are also solutions of the Real Ginzburg–Landau Equation (RGLE),

$$\frac{\partial \psi}{\partial t} = -\frac{\delta \mathcal{F}}{\delta \bar{\psi}} = \alpha \nabla^2 \psi - \psi f'(|\psi|^2). \tag{14}$$

They are thus extrema of the free energy  $\mathcal{F}$ .

The simplest solution of this type corresponds to a constant density fluid at rest. Therefore,  $\psi$  is constant in space and (14) reads

$$f'(|\psi|^2) = -\Omega + \beta|\psi|^2 + 3f_3|\psi|^4 + \dots + nf_n|\psi|^{2n-2} = 0. \tag{15}$$

This equation, for given values of the coefficients  $\beta$  and  $f_i$ ,  $i=3, \dots, n$ , fixes the  $\Omega$  term of  $f$  by the fluid's density  $|\psi|^2$ . However,  $\Omega$  could be removed from the Bernoulli equation (8) by the change of variable  $\varphi \rightarrow \varphi + 2\alpha\Omega t$  that corresponds to a change of phase  $\psi \rightarrow \psi e^{i\Omega t}$  in NLSE (4). Thus,  $\Omega$

does not play an important role in the NLSE dynamics. It is, however, a matter of convention not to perform these changes of variable in order that stationary solutions of (14) coincide with those of (4).

Vortex solutions are another important kind of stationary solutions of NLSE. They are topological defects, or singularities, of Madelung's transformation when  $\rho = 0$  (i.e. when both  $\Re(\psi) = 0$  and  $\Im(\psi) = 0$ ). These two conditions localize singularities into points in two dimensions and lines in three dimensions. The circulation of  $\vec{v}$  around such a generic singularity is  $\pm 4\pi\alpha$ . Therefore, they are known in the framework of superfluidity as *quantum vortices* (Donnelly, 1991). Solutions of (14) with cylindrical symmetry are obtained numerically in Kawatra and Pathria (1966). It is found that the density profile of a vortex admits a horizontal tangent near the core while the velocity diverges as the inverse of the core distance. The momentum density  $\rho\mathbf{v}$  is thus a regular quantity. It is important to realize that such vortex solutions are *regular* solutions of the NLSE (4), the singularity stemming only from Madelung's transformation (5).

### 3. Superfluid turbulence

The mathematical description of superfluid flows (i.e. laboratory  $^4\text{He}$  flows) is based on Landau's two-fluid model (Landau and Lifchitz, 1980). The interaction of normal fluid and superfluid vortices is called *mutual friction* and must be taken into account as pioneered by Schwarz (1985). At sufficiently low temperatures, one can neglect the normal fluid (below  $T = 1$  K for helium at normal pressure) and another mathematical description is given by the NLSE (or Gross–Pitaevskii equation (Gross, 1961; Pitaevskii, 1961)). Note that it is difficult to estimate the precise temperature below which the normal component can be neglected. There remains an urgent need for more experiments at much lower temperatures such as those reported in Davis et al. (2000).

In this section, we will use the simplest form for  $f$ , corresponding to a cubic nonlinearity in the NLSE (4). The NLSE, with convenient normalization, then reads

$$\partial_t \psi = (ic/\sqrt{2}\xi)(\psi - |\psi|^2\psi + \xi^2 \nabla^2 \psi). \quad (16)$$

Madelung's transformation (5) takes the form

$$\rho = |\psi|^2, \quad (17)$$

$$\rho v_j = (ic\xi/\sqrt{2})(\psi \partial_j \bar{\psi} - \bar{\psi} \partial_j \psi), \quad (18)$$

where  $\xi$  and  $c$  are the coherence length defined above and speed of sound (when  $\rho_0 = 1$  [1]), respectively. The superflow is irrotational everywhere but near the lines  $\psi = 0$  (topological defects). There, the flow evolves under Eulerian dynamics (Neu, 1990; Lund, 1991). The topological defect lines are the superfluid vortices, whose velocity circulation is automatically correct in this model (Nozières and Pines, 1990).

The present section is devoted to the analogy between turbulence in low-temperature superfluids and classical turbulence in incompressible viscous fluids. This is done numerically by conducting numerical simulations of NLSE for the Taylor–Green (TG) vortex (Taylor and Green, 1937) and comparing the results with prior Navier–Stokes simulations for the same vortex. The well-documented

TG vortex (Brachet et al., 1983; Brachet, 1990; Domaradzki et al., 1993) is the solution of the Navier–Stokes equations with initial velocity field,

$$\mathbf{v}^{\text{TG}} = (\sin x \cos y \cos z, -\cos x \sin y \cos z, 0). \tag{19}$$

It admits symmetries that are used to speed up computations: rotation by  $\pi$  about the axis ( $x=z=\pi/2$ ), ( $y=z=\pi/2$ ) and ( $x=y=\pi/2$ ) and reflection symmetry with respect to the planes  $x=0, \pi$ ,  $y=0, \pi$ ,  $z=0, \pi$ . The velocity is parallel to these planes which form the sides of the *impermeable box* which confines the flow.

### 3.1. Tools for vortex dynamics

It is well known that compressible fluid dynamics, with an arbitrary chosen initial condition, leads to a flow dominated by acoustic radiation. We must thus generate an initial data with as small acoustic emission as possible if we are to use NLSE to study vortex dynamics.

#### 3.1.1. Preparation method

We now present a method for generating a vortex array whose NLSE dynamics is similar to the classical vortex dynamics of the large-scale flow  $\mathbf{v}^{\text{TG}}$ . Our method has two steps. In the first, we exhibit a global Clebsch representation of  $\mathbf{v}^{\text{TG}}$ . The acoustic wave emission is minimized in the second step (Nore et al., 1994).

The Clebsch potentials,

$$\lambda(x, y, z) = \cos x \sqrt{2 |\cos z|}, \tag{20}$$

$$\mu(x, y, z) = \cos y \sqrt{2 |\cos z|} \operatorname{sgn}(\cos z) \tag{21}$$

(where  $\operatorname{sgn}$  gives the sign of its argument) correspond to the TG flow in the sense that  $\nabla \times \mathbf{v}^{\text{TG}} = \nabla \lambda \times \nabla \mu$  and  $\lambda$  and  $\mu$  are periodic functions of  $(x, y, z)$ . These Clebsch potentials map the physical space  $(x, y, z)$  into the  $(\lambda, \mu)$  plane. The complex field  $\psi_\ell$ , corresponding to the large-scale TG flow circulation, is given by  $\psi_\ell(x, y, z) = (\psi_\ell(\lambda, \mu))^{\lfloor \gamma_d/4 \rfloor}$  with  $\gamma_d = 2\sqrt{2}/(\pi c \xi)$  ( $\lfloor \cdot \rfloor$  denotes the integer part of a real) and

$$\psi_\ell(\lambda, \mu) = \psi_\ell(\lambda - 1/\sqrt{2}, \mu) \psi_\ell(\lambda, \mu - 1/\sqrt{2}) \psi_\ell(\lambda + 1/\sqrt{2}, \mu) \psi_\ell(\lambda, \mu + 1/\sqrt{2}), \tag{22}$$

where  $\psi_\ell(\lambda, \mu) = (\lambda + i\mu) \tanh(\sqrt{\lambda^2 + \mu^2}/\sqrt{2}\xi)/\sqrt{\lambda^2 + \mu^2}$ .

The second step of our procedure consists of integrating, to convergence, the Advective Real Ginzburg–Landau Equation (ARGLE),

$$\partial_t \psi = c/(\sqrt{2}\xi)(\psi - |\psi|^2 \psi + \xi^2 \nabla^2 \psi) - i \mathbf{v}^{\text{TG}} \cdot \nabla \psi - (\mathbf{v}^{\text{TG}})^2/(2\sqrt{2}c\xi) \psi \tag{23}$$

with initial data  $\psi = \psi_\ell$ .

Using the TG symmetries we expand  $\psi(x, y, z, t)$ , a solution of the ARGLE and NLSE equations, as in Nore et al. (1997a):

$$\psi(x, y, z, t) = \sum_{m=0}^{N/2} \sum_{n=0}^{N/2} \sum_{p=0}^{N/2} \hat{\psi}(m, n, p, t) \cos mx \cos ny \cos pz, \tag{24}$$

where  $N$  is the resolution and  $\hat{\psi}(m, n, p, t) = 0$ , unless  $m, n, p$  are either all even or all odd integers. Furthermore  $\hat{\psi}(m, n, p, t)$  satisfies the additional conditions  $\hat{\psi}(m, n, p, t) = (-1)^{r+1} \hat{\psi}(n, m, p, t)$  where

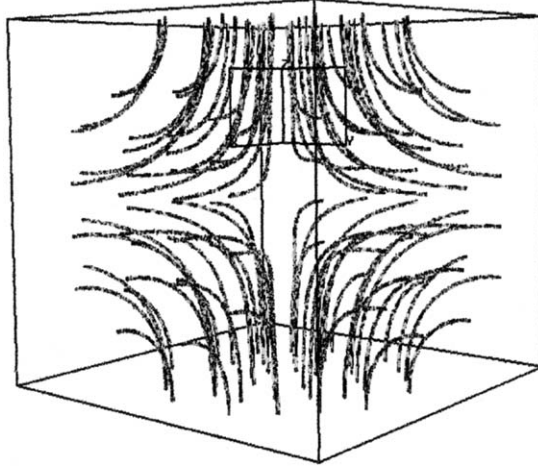


Fig. 1. Three-dimensional visualization of the vector field  $\nabla \times (\rho v)$  for the Taylor–Green flow at time  $t=0$  with coherence length  $\xi = 0.1/(8\sqrt{2})$ , sound velocity  $c = 2$  and  $N = 512$  in the impermeable box  $[0, \pi] \times [0, \pi] \times [0, \pi]$ .

$r = 1$  when  $m, n, p$  are all even and  $r = 2$  when  $m, n, p$  are all odd. Implementing this expansion in a pseudo-spectral code yields a saving of a factor 64 in computational time and memory size when compared to general Fourier expansions.

The ARGLE converged periodic vortex array obtained in this manner is displayed on Fig. 1 with coherence length  $\xi = 0.1/(8\sqrt{2})$ , sound velocity  $c = 2$  and resolution  $N = 512$ .

### 3.1.2. Energy spectra

The total energy of the vortex array, conserved by NLSE dynamics, can be decomposed into three parts  $E_{\text{tot}} = (1/2\pi)^3 \int d^3x (\mathcal{E}_{\text{kin}} + \mathcal{E}_{\text{int}} + \mathcal{E}_q)$ , with kinetic energy  $\mathcal{E}_{\text{kin}} = \rho v_j v_j / 2$ , internal energy  $\mathcal{E}_{\text{int}} = (c^2/2)(\rho - 1)^2$  and quantum energy  $\mathcal{E}_q = c^2 \xi^2 (\partial_j \sqrt{\rho})^2$ . Each of these parts can be defined as the integral of the square of a field, for example,  $\mathcal{E}_{\text{kin}} = (\sqrt{\rho} v_j)^2 / 2$ . In order to separate the kinetic energy corresponding to compressibility effects,  $\mathcal{E}_{\text{kin}}$  can be further decomposed into compressible and an incompressible parts using  $\sqrt{\rho} v_j = (\sqrt{\rho} v_j)^c + (\sqrt{\rho} v_j)^i$  with  $\nabla \cdot (\sqrt{\rho} v_j)^i = 0$ . Using Parseval's theorem, the angle-averaged kinetic energy spectrum is written as

$$E_{\text{kin}}(k) = \frac{1}{2} \int k^2 \sin \theta d\theta d\phi \left| \frac{1}{(2\pi)^3} \int d^3r e^{ir_j k_j} \sqrt{\rho} v_j \right|^2,$$

which satisfies  $E_{\text{kin}} = (\frac{1}{2} \pi)^3 \int d^3x \mathcal{E}_{\text{kin}} = \int_0^\infty dk E_{\text{kin}}(k)$ . The angle-averaged spectrum is obtained by summation over shells in Fourier space. A mode  $(m, n, p)$  belongs to the shell numbered  $k = [\sqrt{m^2 + n^2 + p^2 + \frac{1}{2}}]$ .

Note that the radius of curvature of the vortex lines in Fig. 1 is large compared to their radii. Thus these 3D lines can be considered as straight, and then compared to the 2D axisymmetric vortices which are exact solutions to the 2D NLSE. A 2D vortex at the origin can be written as  $\psi^{\text{vort}}(r) = \sqrt{\rho(r)} \exp(im\varphi)$ ,  $m = \pm 1$ , where  $(r, \varphi)$  are polar coordinates. The vortex profile admits different limits  $\sqrt{\rho(r)} \sim r$  as  $r \rightarrow 0$  and  $\sqrt{\rho(r)} = 1 + O(r^{-2})$  for  $r \rightarrow \infty$ . It can be computed numerically using mapped Chebychev polynomials and an appropriate functional (Nore et al., 1997a).

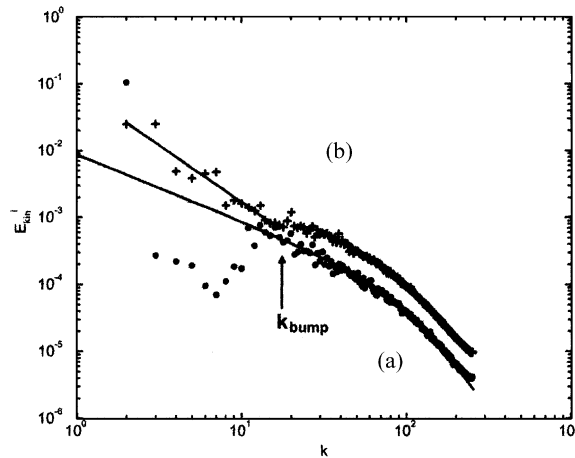


Fig. 2. Plot of the incompressible kinetic energy spectrum,  $E_{\text{kin}}^i(k)$ . The bottom curve (a) (circles) corresponds to time  $t = 0$ . The spectrum of a single axisymmetric 2D vortex multiplied by  $(l/2\pi) = 175$  is shown as the bottom solid line. The top curve (b) (pluses) corresponds to time  $t = 5.5$ . A least-square fit over the interval  $2 \leq k \leq 16$  with a power law  $E_{\text{kin}}^i(k) = Ak^{-n}$  gives  $n = 1.70$  (top solid line).

The corresponding velocity field is azimuthal and is given by  $v(r) = \sqrt{2c\xi}/r$ . Using the mapped Chebychev polynomials expansion for  $\sqrt{\rho(r)}$ , the angle averaged spectrum of  $\sqrt{\rho}v_j$  can then be computed with the formula  $E_{\text{kin}}^{\text{vort}}(k) = (c^2 \xi^2 / 2\pi k) (\int_0^\infty dr J_0(kr) \partial_r \sqrt{\rho})^2$  (Nore et al., 1997a), where  $J_0$  is the zeroth order Bessel function.

The incompressible kinetic energy spectrum  $E_{\text{kin}}^i$  of the ARGLE converged vortex array of Fig. 1 is displayed on Fig. 2. For large wave numbers, the spectrum is well represented by extending a collection of 2D vortices into 3D vortex lines via  $E_{\text{kin}}^{\text{line}}(k) \equiv \text{const.} \times E_{\text{kin}}^{\text{vort}}(k)$ . (We will see that the constant of proportionality is related to the length  $l$  of vortex lines by  $\text{const.} = l/(2\pi) = 175$  at time  $t = 0$ .) In contrast, the small wave number region cannot be represented by  $E_{\text{kin}}^{\text{line}}$ . This stems from the average separation distance between the vortex lines in Fig. 1. Denoting this distance  $d_{\text{bump}} = k_{\text{bump}}^{-1} = \frac{1}{16}$ , the wave number range between the large-scale wave number  $k = 2$  and the characteristic separation wave number  $k_{\text{bump}}$  can be explained by interference effects. Due to constructive interference, the energy spectrum at  $k = 2$  has a value close to its corresponding value in TG viscous flow (namely 0.125), which greatly exceeds the value of  $E_{\text{kin}}^{\text{line}}(k = 2)$ . In contrast, for  $2 < k \leq k_{\text{bump}}$ , destructive interference decreases  $E_{\text{kin}}^i$  below  $E_{\text{kin}}^{\text{line}}$ .

### 3.2. Numerical results

The evolution in time via NLSE (16) of the incompressible kinetic energy is shown in Fig. 3. The main quantitative result is the excellent agreement of the energy dissipation rate,  $-dE_{\text{kin}}^i/dt$ , with the corresponding data in the incompressible viscous TG flow (see Brachet et al. (1983), Fig. 5.12 in Frisch (1995)). Both the moment  $t_{\text{max}} \sim 5-10$  of maximum energy dissipation (the inflection point of Fig. 3) and its value  $\varepsilon(t_{\text{max}}) \sim 10^{-2}$  at that moment are in quantitative agreement. Furthermore, both  $t_{\text{max}}$  and  $\varepsilon(t_{\text{max}})$  depend weakly on  $\xi$ .

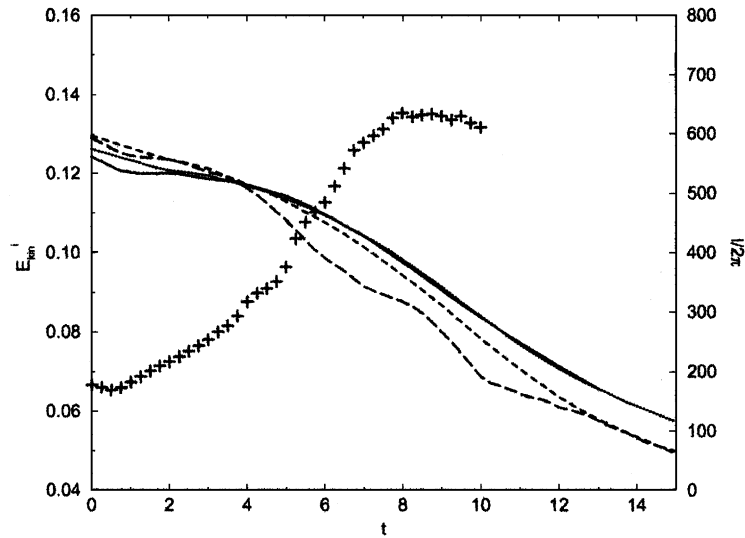


Fig. 3. Total incompressible kinetic energy,  $E_{\text{kin}}^i$ , plotted versus time for  $\zeta = 0.1/(2\sqrt{2})$ ,  $N = 128$  (long-dashed line);  $\zeta = 0.1/(4\sqrt{2})$ ,  $N = 256$  (dashed);  $\zeta = 0.1/(6.25\sqrt{2})$ ,  $N = 400$  (dotted) and  $\zeta = 0.1/(8\sqrt{2})$ ,  $N = 512$  (solid line). All runs are realized with  $c = 2$ . The evolution of the total vortex filament length divided by  $2\pi$  (crosses) for the  $N = 512$  run is also shown (scale given on the right  $y$ -axis).

Another important quantity studied in viscous decaying turbulence is the scaling of the kinetic energy spectrum during time evolution and, especially, at the moment of maximum energy dissipation, where a  $k^{-5/3}$  range can be observed (see Brachet et al. (1983)). Fig. 2 (b) shows the energy spectrum at  $t = 5.5$ . A least-square fit over the interval  $2 \leq k \leq 16$  with a power law  $E_{\text{kin}}^i(k) = Ak^{-n}$  gives  $n = 1.70$  (solid line). For  $5 < t < 8$ , a similar fit gives  $n = 1.6 \pm 0.2$  (data not shown). Note that recent numerical simulations (Araki et al., 2002) using incompressible Eulerian dynamics of vortex filaments also show evidence of a  $k^{-5/3}$  energy spectrum range.

The full Kolmogorov law is given by  $E(k) = C\epsilon^{2/3}k^{-5/3}$  with  $E(k)$  the energy spectrum (per unit mass),  $C$  the Kolmogorov constant and  $\epsilon$  the energy dissipation rate (per unit mass). The viscous energy spectrum  $E(k)$  is comparable (see Brachet et al., 1983), in the inertial range, to the superfluid incompressible kinetic energy  $E_{\text{kin}}^i(k)$ . As stated above, the superfluid dissipation rate  $-dE_{\text{kin}}^i/dt$  is also comparable to the viscous dissipation rate  $\epsilon$ . Therefore, the Kolmogorov constant  $C$  is of the same order of magnitude in both viscous and superfluid flows. Note that the viscous Taylor–Green vortex, because of the inhomogeneous character of the flow, has a Kolmogorov constant that is larger (by a factor  $\simeq 1.5$ ) (Brachet et al., 1983) than that of homogeneous turbulence.

Fitting  $E_{\text{kin}}^i(k)$  in the interval  $30 \leq k \leq 170$  with  $l/(2\pi) \times E_{\text{kin}}^{\text{opt}}(k)$  leads to  $l/2\pi = 452$ , roughly three times the  $t=0$  length of the vortex lines. The time evolution of  $l/2\pi$  obtained by this procedure is displayed in Fig. 3, showing that the length continues to increase beyond  $t_{\text{max}}$ . The computations were performed with  $c=2$  corresponding to a root-mean-square Mach number  $M_{\text{rms}} \equiv |\mathbf{v}_{\text{rms}}^{\text{TG}}|/c = 0.25$ . As it is very costly to decrease  $M_{\text{rms}}$ , we checked (Nore et al., 1997a) that compressible effects were not dominant at this value of  $M_{\text{rms}}$ .

The vortex lines are visualized in physical space in Figs. 4 and 5 at time  $t = 4$  and 8. At  $t = 4$ , no reconnection has yet taken place while a complex vortex tangle is present at  $t = 8$ . Detailed

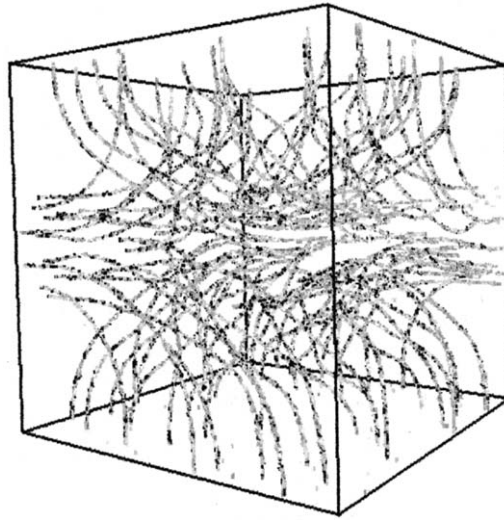


Fig. 4. Same visualization as in Fig. 1 but at time  $t = 4$ .

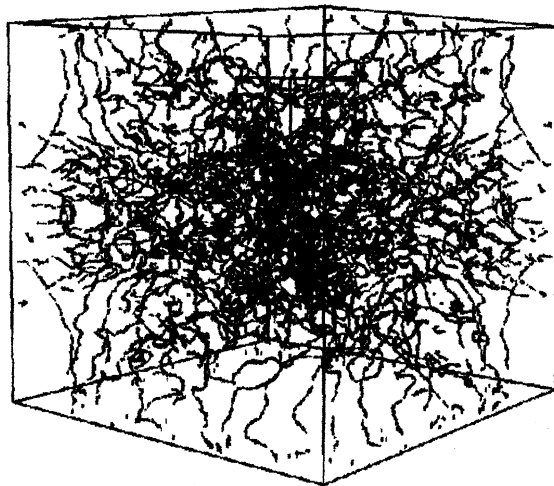


Fig. 5. Same visualization as in Fig. 1 but at time  $t = 8$ .

visualizations (data not shown) demonstrate that reconnections occur for  $t > 5$ . Note that the viscous TG vortex also undergoes a qualitative (and quantitative) change in vortex dynamics around  $t \sim 5$ .

### 3.3. Experimental results

The TG flow is related to an experimentally studied swirling flow (Douady et al., 1991; Fauve et al., 1993; Zocchi et al., 1994). The relation between the experimental flow and the TG vortex is a similarity in overall geometry (Douady et al., 1991): a shear layer between two counter-rotating

eddies. The TG vortex, however, is periodic with free-slip boundaries while the experimental flow is contained inside a tank between two counter-rotating disks.

The spectral behavior of NLSE can be compared to standard (viscous) turbulence only for  $k \leq k_{\text{bump}}$ . It is thus of interest to estimate the scaling of  $k_{\text{bump}}$  in terms of the characteristic parameters of the large-scale flow and of the fluid. As seen above,  $k_{\text{bump}} \sim d_{\text{bump}}^{-1}$ , where  $d_{\text{bump}}$  is the average distance between neighboring vortices. Consider a flow with characteristic integral scale  $l_0$  and large-scale velocity  $u_0$  (in the case of the TG flow,  $l_0 \sim 1$  and  $u_0 \sim 1$ ). The fluid characteristics are the velocity of sound  $c$  and the coherence length  $\xi$  (with corresponding wave number  $k_\xi \sim \xi^{-1}$ ). The number  $n_d$  of vortex lines crossing a typical large-scale  $l_0^2$  area is given by the ratio of the large-scale flow circulation  $l_0 u_0$  to the quantum of circulation  $\Gamma = 4\pi c \xi / \sqrt{2}$ , i.e.  $n_d \sim l_0 u_0 / c \xi$ . On the other hand, the assumption that the vortices are uniformly spread over the large-scale area gives  $n_d \sim l_0^2 / d_{\text{bump}}^2$ . Equating these two evaluations of  $n_d$  yields the relation  $d_{\text{bump}} \sim l_0 \sqrt{(c \xi) / (l_0 u_0)}$ . Note that this argument assumes that the large-scale vorticity is coherent. It, therefore, yields a maximum possible value of  $d_{\text{bump}}$ , and thus a minimum for  $k_{\text{bump}}$ .

In the case of helium, the viscosity at the critical point ( $T = 5.174$  K,  $P = 2.2 \times 10^5$  Pa) is  $\nu_{\text{cp}} = 0.27 \times 10^{-7} \text{ m}^2 \text{ s}^{-1}$  while the quantum of circulation,  $\Gamma = h/m_{\text{He}}$  has the value  $0.99 \times 10^{-7} \text{ m}^2 \text{ s}^{-1}$ . Thus,  $\nu_{\text{cp}} \sim 0.25\Gamma$ . The order of magnitude for  $d_{\text{bump}}$  is thus  $d_{\text{bump}} \simeq l_0 / \sqrt{R_{\text{cp}}} \sim l_\lambda$  where  $R_{\text{cp}}$  is the integral scale Reynolds number at the critical point and  $l_\lambda$  the Taylor micro-scale. In other words, the value of  $d_{\text{bump}}$  in a superfluid helium experiment at  $T = 1$  K is of the same order as the Taylor micro-scale in the same experimental set-up run with viscous helium at the critical point.

The experimental set-up is similar to that described in Zocchi et al. (1994). To work with  $T \sim 1.2$  K some modifications are, however, necessary. A cylinder, 8 cm in diameter and 12 cm high, limited axially by two counter-rotating disks limits the flow. One disk is flat and 8 radial blades, forming an angle of  $45^\circ$  between each other, are fixed on the other one. To stabilize the turbulent shear region a stator is mounted at half the height of the container. The two disks are driven by two DC motors rotating from 1 to 30 Hz. The whole system is enclosed in a liquid Helium bath used as the experimental fluid and this is the main difference with the set-up described in Zocchi et al. (1994). The pressure above the liquid bath is adjusted by a pumping system and this fixes the temperature of the fluid.

Local pressure fluctuations are measured by using small total-head pressure tubes, immersed in the flow. The pressure sensors are hollow metallic tubes, connected to a quartz pressure transducer WHM 112 A22 from PCB. Details are given in Abid et al. (1998).

In normal fluids, the pressure measured at the tip of the total-head tube can be related to the upstream flow  $U(t)$  and the local pressure  $P(t)$  using Bernoulli's theorem,

$$P_{\text{meas}}(t) = P(t) + \rho U^2(t)/2. \quad (25)$$

In the flow region where the probe is immersed, a well established axial mean flow  $U$  exists so that, after removing the mean parts of Eq. (25), one gets

$$p_{\text{meas}}(t) = p(t) + \rho U u(t), \quad (26)$$

where  $p_{\text{meas}}$ ,  $p$  and  $u$  are the fluctuations of the measured pressure, the actual pressure, and the local velocity, respectively. It is currently admitted that, in ordinary turbulent situations, and at low fluctuation rates, Eq. (26) is dominated by the dynamic term, so that, by measuring the pressure fluctuations at the total head tube, one has a direct access to the velocity fluctuations  $u(t)$ .

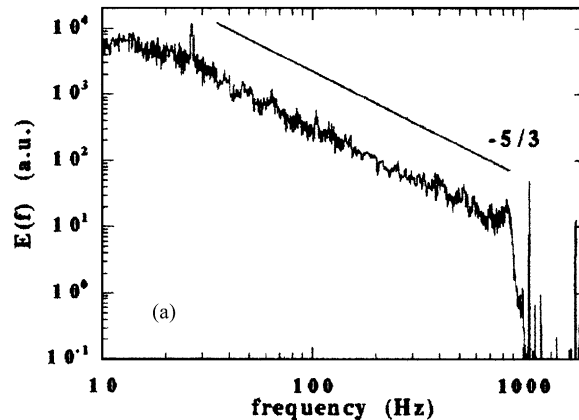


Fig. 6. Experimental pressure fluctuation spectrum (in nondimensional units) measured with a total head pressure tube immersed in the flow at  $T = 2.3$  K.

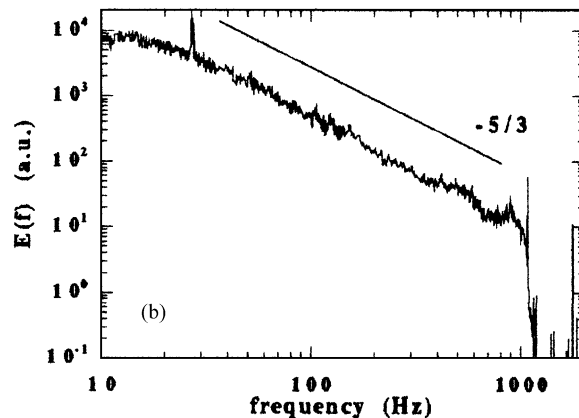


Fig. 7. Experimental pressure fluctuation spectrum (in nondimensional units) measured with a total head pressure tube immersed in the flow at  $T = 1.4$  K.

The situation is less clear when the probe is immersed in the superfluid. It is, however, possible to write an equation similar to (26). Details can be found in Abid et al. (1998).

The analysis of the pressure fluctuations obtained with the total head tube placed at 2 cm above the mid plane and 2 cm from the cylinder axis, yields interesting conclusions. Figs. 6 and 7 show the spectra of the pressure fluctuations above and below  $T_\lambda$  (i.e., respectively, at 2.3 and 1.4 K). Fig. 6 clearly shows, as expected, that such fluctuations follow a Kolmogorov regime between the injection scale (signaled by the peak at 25 Hz) and the largest resolved frequency, i.e. 900 Hz. The spectrum obtained at 1.4 K is similar to that obtained at  $T = 2.3$  K (see Fig. 7). A clear Kolmogorov like regime exists for the same range of frequencies. The corresponding Kolmogorov constant turns out also to be indistinguishable from the classical value. We have further analyzed the deviations from Kolmogorov in the superfluid regime. The striking result is that they have the same magnitude as in classical turbulence. More details are given in Maurer and Tabeling (1998).

These observations—both on global and local quantities—agree well with the theoretical approach developed in the previous section. In particular, it seems clear that the Kolmogorov cascade survives in the superfluid regime.

#### 4. Stability of stationary solutions

This section is devoted to the stability of Bose-Einstein condensates (BEC). Exact 1D bifurcation results are given in Section 4.1. A general formulation of stability is presented in Section 4.2. Numerical branch following methods are explained in Section 4.3. The stability of a superflow around a cylinder is investigated in Section 4.4 and attractive Bose–Einstein condensates are studied in Section 4.5.

##### 4.1. Exact solution in 1D

###### 4.1.1. Definition of the system

We consider a point impurity moving within a 1D superflow. In the frame of the moving impurity, the system can be described by the following action functional:

$$\mathcal{A}[\psi, \bar{\psi}] = \int dt \left[ \frac{i}{2} \int dx (\bar{\psi} \partial_t \psi - \psi \partial_t \bar{\psi}) - \mathcal{H} \right]. \quad (27)$$

In this expression,  $\psi$  is a complex field,  $\bar{\psi}$  its conjugate and the energy functional  $\mathcal{H}$  reads

$$\mathcal{H} = \mathcal{E} - v\mathcal{P} + v[R^2(+\infty)\phi(+\infty) - R^2(-\infty)\phi(-\infty)] \quad (28)$$

with

$$\mathcal{E} = \int dx [|\partial_x \psi|^2 + \frac{1}{2}(|\psi|^2 - 1)^2 + g\delta(x)(|\psi|^2 - 1)], \quad (29)$$

$$\mathcal{P} = \int dx \frac{1}{2i} [\bar{\psi}(\partial_x \psi) - \psi(\partial_x \bar{\psi})], \quad (30)$$

$$\psi = R \exp(i\phi). \quad (31)$$

The Dirac (pseudo) potential  $g\delta(x)$  in (29) represents the impurity and the last term in (28) imposes the appropriate boundary conditions for the phase  $\phi$  (Hakim, 1997).  $R$  obeys the boundary conditions  $R^2(\pm\infty) = 1$ .

The Euler–Lagrange equation associated to (27),  $\delta\mathcal{A}/\delta\bar{\psi} = 0$ , is the nonlinear Schrödinger equation (NLSE)

$$i\partial_t \psi = -\partial_{xx} \psi + iv\partial_x \psi - \psi + |\psi|^2 \psi + g\delta(x)\psi, \quad (32)$$

where the jump condition

$$\partial_x \psi(0^+, t) - \partial_x \psi(0^-, t) = g\psi(0, t) \quad (33)$$

is imposed in order to balance the  $g\delta(x)\psi$  singularity with the  $-\partial_{xx}\psi$  term for all times  $t$ .

#### 4.1.2. Stationary solutions

Time-independent solutions of the NLSE (32) are best studied by performing the change of variables defined above in (31):  $\psi = R \exp(i\phi)$ . Using these variables, the NLSE reads

$$\partial_t R = v \partial_x R - R \partial_{xx} \phi - 2 \partial_x R \partial_x \phi, \tag{34}$$

$$\partial_t \phi = v \partial_x \phi - (\partial_x \phi)^2 + 1 - R^2 - g \delta(x) + \frac{\partial_{xx} R}{R}, \tag{35}$$

and the jump condition (33) reads

$$\partial_x R(0^+, t) - \partial_x R(0^-, t) = gR(0, t), \tag{36}$$

$$\partial_x \phi(0^+, t) - \partial_x \phi(0^-, t) = 0. \tag{37}$$

Note that Eqs. (34) and (35) can be, respectively, interpreted as the continuity and Bernoulli equations for a fluid of density  $\rho = R^2(x)$  and velocity  $u = 2 \partial_x \phi$  (as done in Section 2).

Explicit time-independent solutions of (34) and (35) were found by Hakim (1997), using what are called *gray solitons* in the nonlinear optics terminology. Gray solitons (Tsuzuki, 1971; Zakharov and Shabat, 1973) are stationary solutions of (34) and (35), *without* the potential term  $g\delta(x)$ . They are localized density depletion of the form

$$R_{GS}(x) = v^2/2 + (1 - v^2/2) \tanh^2 \left[ \sqrt{1/2 - v^2/4} x \right], \tag{38}$$

$$\phi_{GS}(x) = \arctan \left( \frac{v \sqrt{2 - v^2}}{\exp \left[ \sqrt{2 - v^2} x \right] + v^2 - 1} \right). \tag{39}$$

Patching together pieces of gray solitons, Hakim found the following  $\xi$ -indexed stationary solutions of Eqs. (34) and (35), *including* the potential term  $g\delta(x)$

$$R_\xi(x) = R_{GS}(x \pm \xi) \quad (x \gtrless 0), \tag{40}$$

$$\phi_\xi(x) = \phi_{GS}(x \pm \xi) - \phi_{GS}(\pm \xi) \quad (x \gtrless 0), \tag{41}$$

where the jump conditions (36) and (37) impose the relation

$$g(\xi) = \sqrt{2}(1 - v^2/2)^{3/2} \frac{\tanh \left[ \sqrt{1/2 - v^2/4} \xi \right]}{v^2/2 + \sinh^2 \left[ \sqrt{1/2 - v^2/4} \xi \right]}. \tag{42}$$

The function  $g(\xi)$  reaches a maximum (Pham and Brachet, 2002)  $g_c = g(\xi_c)$  at  $\xi_c = \text{argcosh}(1 + \sqrt{1 + 4v^2/2})/(\sqrt{2 - v^2})$  with

$$g_c = 4(1 - v^2/2) \frac{\left[ \sqrt{1 + 4v^2} - (1 + v^2) \right]^{1/2}}{2v^2 - 1 + \sqrt{1 + 4v^2}}. \tag{43}$$

The two stationary solutions of (32) corresponding to  $\xi_+(g) > \xi_c$  and  $\xi_-(g) < \xi_c$  obtained by inverting (42) for  $g < g_c$  thus disappear, merging in a saddle-node bifurcation at a critical strength  $g_c$ .

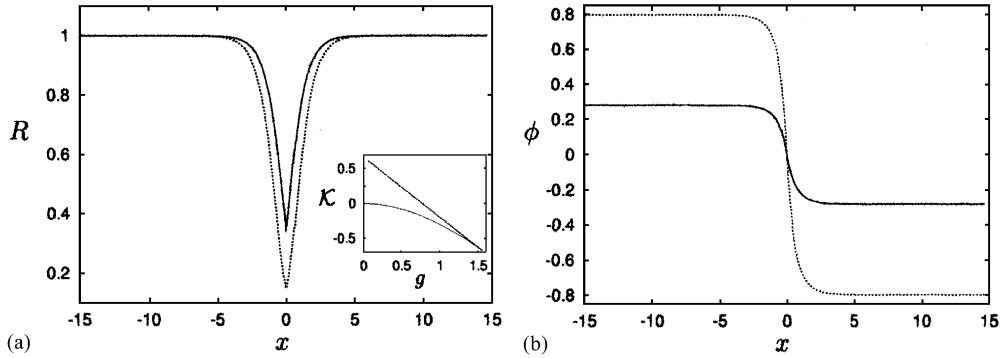


Fig. 8. (a) Modulus  $R$  of the stable (—) and unstable (---) stationary solutions of (32) (see (40)) for  $g = 1.250$  and  $v = 0.5$ ; insert, energy functional  $\mathcal{K}$  of the stationary solutions versus  $g$  for  $v = 0.5$  (see (28)); lower branch: energetically stable branch, upper branch: energetically unstable branch. The bifurcation occurs at  $g = 1.5514$  (b) Phase  $\phi$  of the stable (—) and unstable (---) stationary solutions (see (41)), same conditions as in (a).

Note that the bifurcation can also be obtained by varying  $v$  and keeping  $g$  constant. In the following, the strength  $g$  of the delta function is used as the control parameter of our system, keeping  $v$  constant.

Fig. 8a shows the energetically unstable and stable solutions ( $\mathcal{K}(\xi_-(g)) > \mathcal{K}(\xi_+(g))$ ). The bifurcation diagram corresponding to the energy  $\mathcal{K}$  (see (28)) is also displayed on the figure as an insert. In Fig. 8b, note that the phase  $\phi_\xi(x)$ , as defined in (41), differs from that considered in Hakim (1997) by an ( $x$ -independent) constant. The phase in Hakim (1997) is set to 0 at  $x = +\infty$ , whereas (41) is antisymmetric in  $x$ . This difference is unimportant because (34) and (35) are invariant under the constant phase shift

$$\phi(x) \mapsto \phi(x) + \varphi. \tag{44}$$

#### 4.2. General formulation

In this section, we define and test the numerical tools needed to obtain the stationary solutions of the NLSE.

Consider the following action functional associated with the NLSE,

$$\mathcal{A} = \int d\tilde{t} \left\{ \int d\tilde{\mathbf{x}} \frac{i}{2} \left( \bar{\psi} \frac{\partial \psi}{\partial \tilde{t}} - \psi \frac{\partial \bar{\psi}}{\partial \tilde{t}} \right) - \mathcal{F} \right\}, \tag{45}$$

where  $\psi$  is a complex field,  $\bar{\psi}$  its conjugate and  $\mathcal{F}$  is the energy of the system. Here,  $\mathbf{x}$  and  $\tilde{t}$  correspond to nondimensionalized space and time variables, respectively.

The Euler–Lagrange equation corresponding to (45) leads to the NLSE in terms of the functional  $\mathcal{F}$ ,

$$\frac{\partial \psi}{\partial \tilde{t}} = -i \frac{\delta \mathcal{F}}{\delta \bar{\psi}}. \tag{46}$$

This equation obviously has stationary solution  $\psi_S$  if  $\delta \mathcal{F} / \delta \psi|_{\psi=\psi_S} = 0$ . Thus, stationary solutions of (46) are extrema of  $\mathcal{F}$ . In general, we are looking for an extremum of an energy functional

$\mathcal{E}$  under some constraint  $\mathcal{Q}[\psi] = \text{cst}$ . The usual Lagrange multiplier trick consists in introducing a control parameter  $v$  and, rather than solving for extrema of  $\mathcal{E}[\psi]$ , searching for extrema of the new functional  $\mathcal{F}[\psi] = \mathcal{E}[\psi] - v\mathcal{Q}[\psi]$ . We thus solve for

$$\left. \frac{\delta \mathcal{F}}{\delta \psi} \right|_{v=\text{cst.}} = 0. \tag{47}$$

We now turn to the precise definitions, corresponding to the two systems considered in this section: superflows and Bose–Einstein condensates.

#### 4.2.1. Superflows

In the problem of a superflow past an obstacle,  $\mathcal{E}$  is the hydrodynamic energy and  $v \equiv \mathbf{U}$  is the flow velocity with respect to the obstacle (Huepe and Brachet, 1997; Nore et al., 2000). This implies that  $\mathcal{Q} \equiv \mathbf{P}$  is the flow momentum. Functionals  $\mathcal{F}$ ,  $\mathcal{E}$  and  $\mathbf{P}$  are given by the expressions

$$\mathcal{F} = \mathcal{E} - \mathbf{P} \cdot \mathbf{U}, \tag{48}$$

$$\mathcal{E} = c^2 \int d^3x \left( [-1 + V(\vec{x})] |\psi|^2 + \frac{1}{2} |\psi|^4 + \xi^2 |\nabla \psi|^2 \right), \tag{49}$$

$$\mathbf{P} = \sqrt{2}c\xi \int d^3x \frac{i}{2} (\psi \nabla \bar{\psi} - \bar{\psi} \nabla \psi). \tag{50}$$

Here,  $c$  and  $\xi$  are the physical parameters characterizing the superfluid. They correspond to the speed of sound ( $c$ ) for a fluid with mean density  $\rho_0 = 1$ , and to the coherence length ( $\xi$ ). The potential  $V(\mathbf{x}) = (V_0/2)(\tanh[4(r - D/2)/\Delta] - 1)$  is used to represent a cylindrical obstacle of diameter  $D$ . The computations are performed with  $V_0 = 10$  and  $\Delta = \xi$  for which the density  $|\psi| \sim 0$  in the disk. The NLSE reads

$$\frac{\partial \psi}{\partial t} = -\frac{i}{\sqrt{2}c\xi} \frac{\delta \mathcal{F}}{\delta \bar{\psi}} = i \frac{c}{\sqrt{2}\xi} ([1 - V(\vec{x})]\psi - |\psi|^2\psi + \xi^2 \nabla^2 \psi) + \mathbf{U} \cdot \nabla \psi. \tag{51}$$

We will be interested in the solutions of  $\delta \mathcal{F} / \delta \bar{\psi} = 0$ , for a given value of  $\mathbf{U}$ . According to Eq. (47), these solutions are extrema of  $\mathcal{E}$  at constant momentum  $\mathbf{P}$ .

#### 4.2.2. Bose–Einstein condensates

We consider a condensate of  $\mathcal{N}$  particles of mass  $m$  and effective scattering length  $a$  in a radial confining harmonic potential  $V(r) = m\omega^2 r^2/2$  (Huepe et al., 1999). Quantities are rescaled by the natural quantum harmonic oscillator units of time  $\tau_0 = 1/\omega$  and length  $L_0 = \sqrt{\hbar/m\omega}$ , thus obtaining the nondimensionalized variables  $\tilde{t} = t/\tau_0$ ,  $\tilde{\mathbf{x}} = \mathbf{x}/L_0$  and  $\tilde{a} = 4\pi a/L_0$ . The control parameter  $v$  becomes in this context the chemical potential  $\mu$ . The total number of particles in the condensate is therefore given by  $\mathcal{Q} \equiv \mathcal{N}$ . Functionals  $\mathcal{F}$ ,  $\mathcal{E}$  and  $\mathcal{N}$  are given, in terms of rescaled variables, by

$$\mathcal{F} = \mathcal{E} - \mu \mathcal{N}, \tag{52}$$

$$\mathcal{E} = \int d^3\tilde{\mathbf{x}} \left( \frac{1}{2} |\nabla_{\tilde{\mathbf{x}}}\psi|^2 + V(\tilde{\mathbf{x}})|\psi|^2 + \frac{\tilde{a}}{2} |\psi|^4 \right), \quad (53)$$

$$\mathcal{N} = \int d^3\tilde{\mathbf{x}} |\psi|^2. \quad (54)$$

Two different situations are possible, depending on the sign of the (rescaled) effective scattering length  $\tilde{a}$ . When  $\tilde{a}$  is positive, the particles interact repulsively. A negative  $\tilde{a}$  corresponds to an attractive interaction. The dynamical equation is

$$\frac{\partial\psi}{\partial\tilde{t}} = -i \frac{\delta\mathcal{F}}{\delta\bar{\psi}} = i \left[ \frac{1}{2} \nabla_{\tilde{\mathbf{x}}}^2\psi - \frac{1}{2} |\tilde{\mathbf{x}}|^2\psi - (\tilde{a}|\psi|^2 - \mu)\psi \right]. \quad (55)$$

We will be interested in the solutions of  $\delta\mathcal{F}/\delta\bar{\psi} = 0$ , for a given value of  $\mu$ . According to Eq. (47), these solutions are extrema of  $\mathcal{E}$  at constant particle number  $\mathcal{N}$ .

### 4.3. Branch following methods

When the extremum of  $\mathcal{F}$  is a local *minimum*, the stationary solution  $\psi_s$  of (51) can be reached by a relaxation method. If the extremum is not a minimum, Newton's iterative method is used to solve for  $\psi_s$ .

#### 4.3.1. Relaxation method

In what remains of this section, we will write the NLSE under the following generic form, which is valid for both the Bose–Einstein condensates and the superflow past an obstacle:

$$\frac{\partial\psi}{\partial t} = -i \frac{\delta\mathcal{F}}{\delta\bar{\psi}} = i(\alpha\nabla^2\psi + [\Omega - V(\vec{x})]\psi - \beta|\psi|^2\psi) + \mathbf{U} \cdot \nabla\psi. \quad (56)$$

When the extremum of  $\mathcal{F}$  is a local *minimum*, the stationary solution  $\psi_s$  of (56) can be reached by integrating to relaxation the associated RGLE

$$\frac{\partial\psi}{\partial t} = -\frac{\delta\mathcal{F}}{\delta\bar{\psi}} = \alpha\nabla^2\psi + [\Omega - V(\vec{x})]\psi - \beta|\psi|^2\psi - i\mathbf{U} \cdot \nabla\psi. \quad (57)$$

Indeed, (56) and (57) have the same stationary solutions.

In our numerical computations, Eq. (57) is integrated to convergence by using the Forward–Euler/Backwards–Euler time stepping scheme

$$\psi(t + \sigma) = \Theta^{-1}[(1 - i\sigma\mathbf{U} \cdot \nabla) + \sigma([\Omega - V(\vec{x})] - \beta|\psi(t)|^2)]\psi(t) \quad (58)$$

with

$$\Theta = [1 - \sigma\alpha\nabla^2]. \quad (59)$$

The advantage of this method is that it converges to the stationary solution of (56) independently of the time step  $\sigma$ .

#### 4.3.2. Newton's method

We use Newton's method (Seydel, 1988) to find unstable stationary solutions of the RGLE.

In order to work with a well-conditioned system (Mamun and Tuckerman, 1995), we search for the fixed points of (58). These can be found as the roots of

$$f(\psi) = \Theta^{-1}[(1 - i\sigma \mathbf{U} \cdot \nabla) + \sigma([\Omega - V(\vec{x})] - \beta|\psi(t)|^2)]\psi(t) - \psi(t), \tag{60}$$

where  $\Theta^{-1}$  was already introduced in (58).

We denote by  $\psi_{(j)}$  the value of the field  $\psi$  at the  $j$ th collocation point. The roots of  $f(\psi)$  are found by solving the linear problem

$$\sum_k \left[ \frac{df_{(j)}}{d\psi_{(k)}} \right] \delta\psi_{(k)} = -f_{(j)}(\psi). \tag{61}$$

for  $\delta\psi$  and then incrementing  $\psi$  by

$$\psi_{(j)} = \psi_{(j)} + \delta\psi_{(j)} \tag{62}$$

and iterating the Newton process (61) and (62) to convergence.

The solution to (61) is obtained by an iterative bi-conjugate gradient method, either BCGM (Press et al., 1994) or BiCGSTAB (van der Vorst, 1992). These methods require only the ability to act repeatedly with  $[df_{(j)}/d\psi_{(k)}]$  on an arbitrary field  $\varphi$  to obtain an approximative solution of (61). Note that since the convergence of the time step (58) does not depend on  $\sigma$ , the roots found through this Newton iteration are also independent of  $\sigma$ . Therefore,  $\sigma$  becomes a free parameter that can be used to adjust the preconditioning of the system in order to optimize the convergence of the BCGM (Mamun and Tuckerman, 1995).

### 4.3.3. Implementation

We use standard Fourier pseudo spectral methods (Gottlieb and Orszag, 1977). Typical convergences of the Newton and bi-conjugate gradient iterations are shown in Figs. 9 and 10.

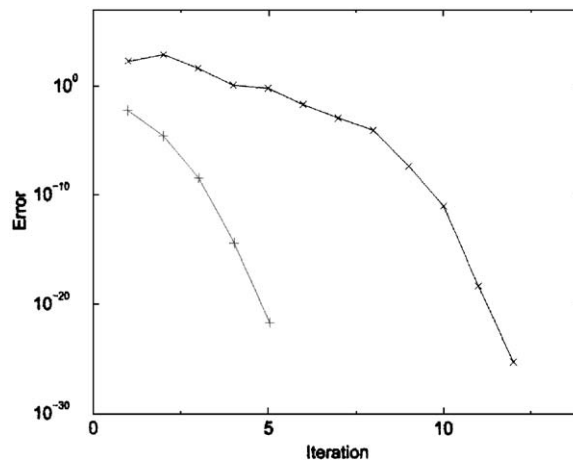


Fig. 9. Two typical examples of the Newton method convergence towards the solution of Eq. (60) for the problem of a superflow past a cylinder with  $\zeta/D = \frac{1}{10}$  and a field  $\psi_{(j)}$  discretized into  $n = 128 \times 64 = 8190$  collocation points. The error measure is given by  $\sum_{j=1}^n f_{(j)}^2(\psi)/n$ . The convergence is faster than exponential, as expected for a Newton method.

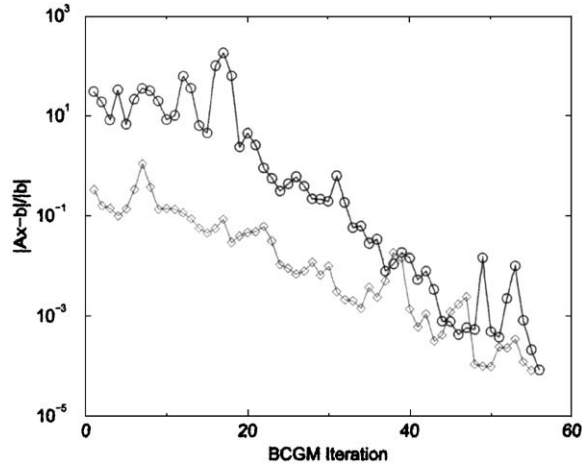


Fig. 10. Two typical examples of a bi-conjugate gradient method convergence corresponding to the case shown in Fig. 9. The convergence of the relative error achieved for the  $\mathbf{x}$  solution of  $\mathbf{Ax}=\mathbf{b}$  is given by  $|\mathbf{Ax}-\mathbf{b}|/|\mathbf{b}|$ , where  $\mathbf{A}=[df_{(j)}/d\psi_{(k)}]$ ,  $\mathbf{b}=-f_{(j)}(\psi)$  and  $\mathbf{x}=\delta\psi_{(k)}$ .

In the case of the radially symmetric Bose condensate,  $\psi(r, \tilde{t})$  is expanded as  $\psi(r, \tilde{t}) = \sum_{n=0}^{N_R/2} \hat{\psi}_{2n}(\tilde{t})T_{2n}(r/R)$ , where  $T_n$  is the  $n$ th order Chebychev polynomial and  $\hat{\psi}_{N_R}$  is fixed to satisfy the boundary condition  $\psi(R, \tilde{t}) = 0$ .

The NLSE is integrated in time by a fractional step (operator-splitting) method (Klein and Majda, 1991).

#### 4.4. Stability of a superflow around a cylinder

In this section, following references (Huepe and Brachet, 1997, 2000; Nore et al., 2000), we investigate the stationary stable and unstable (nucleation) solutions of the NLSE describing the superflow around a cylinder, using the numerical methods developed in Section 4.3. We study a disc of diameter  $D$ , moving at speed  $\mathbf{U}$  in a two-dimensional (2D) superfluid at rest. The NLSE (51) can be mapped into two hydrodynamical equations by applying Madelung’s transformation (Spiegel, 1980; Donnelly, 1991),

$$\psi = \sqrt{\rho} \exp\left(\frac{i\phi}{\sqrt{2}c\xi}\right). \tag{63}$$

The real and imaginary parts of the NLSE produce for a fluid of density  $\rho$  and velocity

$$\mathbf{v} = \nabla\phi - \mathbf{U} \tag{64}$$

the following equations of motion:

$$\frac{\partial\rho}{\partial t} + \nabla(\rho\mathbf{v}) = 0, \tag{65}$$

$$\left[\frac{\partial\phi}{\partial t} - \mathbf{U} \cdot \nabla\phi\right] + \frac{1}{2}(\nabla\phi)^2 + c^2[\rho - (1 - V(\vec{x}))] - c^2\xi^2 \frac{\nabla^2\sqrt{\rho}}{\sqrt{\rho}} = 0. \tag{66}$$

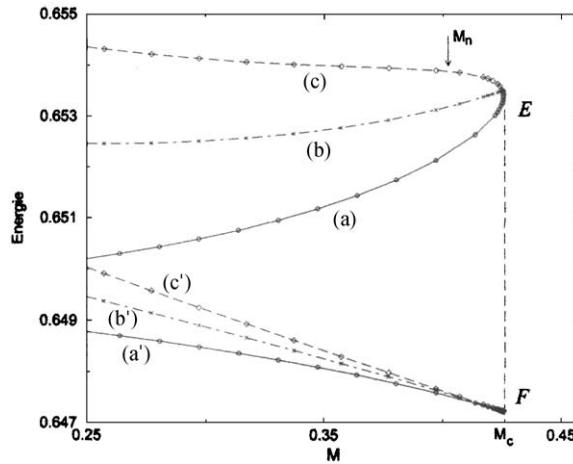


Fig. 11. Plot of the energy ( $\mathcal{F}$ ), and functional ( $\mathcal{E}$ ) versus Mach number ( $M = |U|/c$ ), with  $D = 10\xi$ . Stable state (a). Nucleation solutions: asymmetric branch (b) and symmetric branch (c). The diagram shows a saddle-node and a pitchfork bifurcation. The point where vortices cross the surface of the disc (see Fig. 12) is labeled by  $M_n$ . The total fluid momentum is given by  $-d\mathcal{F}/dU$  (see text).

In the coordinate system  $\vec{x}$  that follows the obstacle, these equations correspond to the continuity equation and to the Bernoulli equation (Landau and Lifchitz, 1980) (with a supplementary *quantum pressure* term  $c^2 \xi^2 \nabla^2 \sqrt{\rho}/\sqrt{\rho}$ ) for an isentropic, compressible and irrotational flow. Note that, in the limit where  $\xi/D \rightarrow 0$ , the quantum pressure term vanishes and we recover the system of equations describing an Eulerian flow.

#### 4.4.1. Bifurcation diagram and scaling in 2D

In this section, varying the ratio of the coherence length  $\xi$  to the cylinder diameter  $D$ , we obtain scaling laws in the  $\xi/D \rightarrow 0$  limit.

*Bifurcation diagram:* We present results for  $\xi/D = \frac{1}{10}$  which are representative of all ratios we computed. The functional  $\mathcal{E}$  and energy  $\mathcal{F}$  of the stationary solutions are shown in Fig. 11 as a function of the Mach number ( $M = |U|/c$ ). The stable branch (a) disappears with the unstable solution (c) at a saddle-node bifurcation when  $M = M^c \approx 0.4286$ . The energy  $\mathcal{F}$  has a cusp at the bifurcation point, which is the generic behavior for a Hamiltonian saddle-node bifurcation, as described in Section 4.5.1. There are no stationary solutions beyond this point. When  $M^{pf} \approx 0.4282$ , the unstable symmetric branch (c) bifurcates at a pitchfork to a pair of asymmetric branches (b). Their nucleation energy barrier is given by  $(\mathcal{F}_b - \mathcal{F}_{a'})$  which is roughly half of the barrier for the symmetric branch  $(\mathcal{F}_c - \mathcal{F}_{a'})$ .

We can relate branches in Fig. 11 to the presence of vortices in the solution. When  $M^n \leq M \leq M^c$ , solutions are irrotational ( $M^n \sim 0.405$  as indicated in Fig. 11). For  $M \leq M^n$  the stable branch (a) remains irrotational (Fig. 12A) while the unstable branch (b) corresponds to a one vortex solution (Fig. 12B) and the unstable branch (c), to a two-vortex solution (Fig. 12C). The distance between the vortices and the obstacle in branches (b) and (c) increases when  $M$  is decreased. Branch (c) is precisely the situation described in Frisch et al. (1992). Furthermore, the value  $M^c \approx 0.4286$  is close

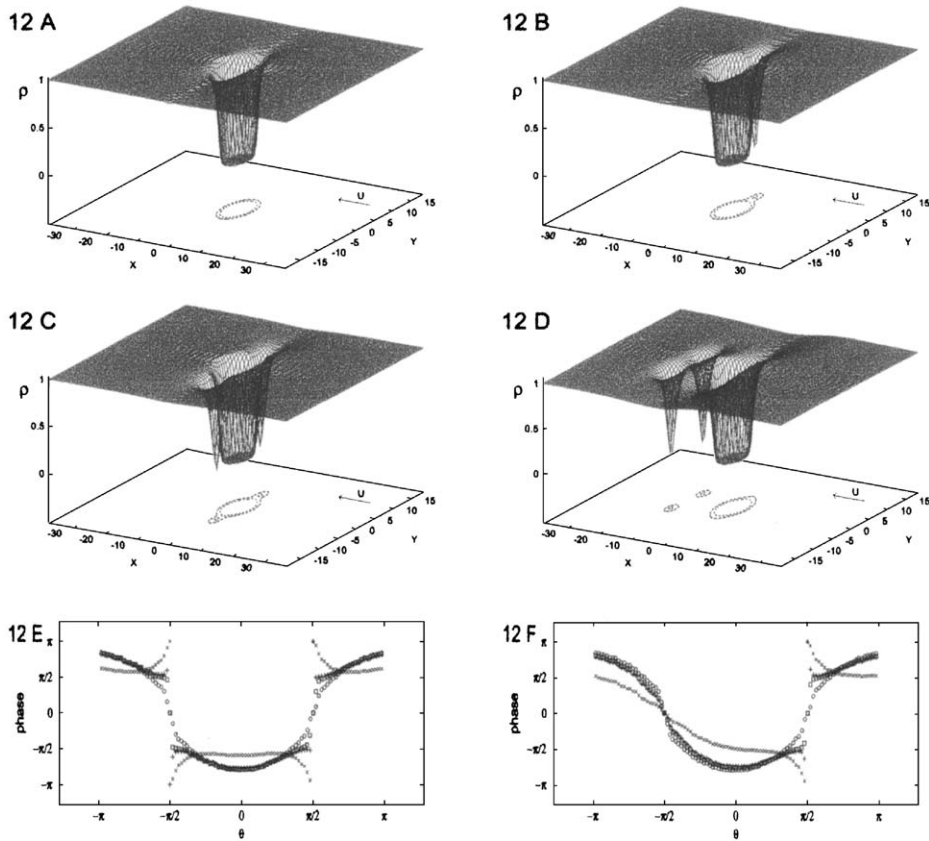


Fig. 12. Stationary state: stable state (A), one vortex unstable state (B), two vortex unstable state (C). The surface indicates the fluid density around the cylinder ( $M = 0.24$ ,  $\xi/D = 0.1$ ). Figure (D) shows the result of the NLSE integration, starting from a slightly perturbed stationary (C) state. Figures (E) and (F) display the phase of the complex field  $\psi$  at the surface of the cylinder versus the polar angle  $\theta$ . Symmetric branch (E), asymmetric branch (F).  $M = 0.4286$  ( $\circ$ ),  $M = 0.41$  ( $\square$ ),  $M = 0.40$  ( $+$ ),  $M = 0.30$  ( $\times$ ). The crossing out of the vortex produces a phase discontinuity at  $M^n \sim 0.405$ .

to the predicted value  $\sqrt{2/11}$ . Fig. 12D shows the result of integrating the NLSE forward in time with, as initial condition, a slightly perturbed unstable symmetric stationary state (Fig. 12C). The perturbation drives the system over the nucleation barrier and cycles it, after the emission of two vortices, back to a stationary stable solution. This shows that branch (c) corresponds to hyperbolic fixed points of NLSE.

Figs. 12E and F show the phase of the field at the surface of the disc ( $r = D/2$  and  $\theta \in [0, 2\pi]$ ) for four different flow speeds. In both unstable branches,  $2\pi$ -discontinuities, a diagnostic of vortex crossing, appear between  $M = 0.40$  and  $0.41$ .

*Scaling laws:* We now characterize the dependence on  $\xi/D$  of the main features of the bifurcation diagram. When  $\xi/D$  is decreased,  $M^c$  and  $M^{pf}$  become indistinguishable. In the limit where  $\xi/D = 0$ , the critical Mach number  $M^c$  will be that of an Eulerian flow  $M_{\text{Euler}}^c$ .

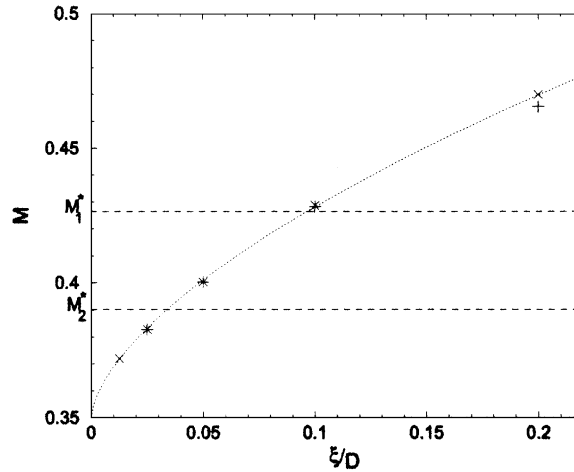


Fig. 13. Saddle-node bifurcation Mach number  $M^c$  (+) and pitchfork bifurcation Mach number  $M^{pf}$  ( $\times$ ), as a function of  $\xi/D$ . The dotted curve corresponds to a fit to the polynomial law  $M^c = K_1(\xi/D)^{K_2} + M_{Euler}^c$  with  $K_1 = 0.322$ ,  $K_2 = 0.615$  and  $M_{Euler}^c = 0.35$ .

Fig. 13 shows the convergence of  $M^c$  to the Eulerian critical velocity. This convergence can be characterized by fitting the polynomial law  $M^c = K_1(\xi/D)^{K_2} + M_{Euler}^c$  to  $M^c(\xi/D)$ . This fit is shown in Fig. 13 as a dotted line, yielding  $K_1 = 0.322$ ,  $K_2 = 0.615$  and  $M_{Euler}^c = 0.35$ .

*Dynamical solutions:* The stationary solutions obtained in the above subsection provide adequate initial data for the study of dynamical solutions. Indeed, after a small perturbation, their integration in time will generate a dynamical evolution with very small acoustic emission. Therefore, this procedure is an efficient way to initialize vortical dynamics in a controlled manner.

Starting from a two-vortex unstable stationary solution at a supercritical Mach number  $M^c = 0.9$ , the evolution of the NLSE time integration shows a clearly periodic emission of vortex pairs (see Fig. 12D). This emission conserves total circulation.

We have studied the behavior of the frequency of vortex emission close to the bifurcation for these symmetric wakes with different supercritical velocities (characterized by  $\delta_{sp} = (M - M^c)/M^c = -\delta > 0$ ). Our results, plotted in Fig. 14, are consistent with a  $\delta_{sp}^{1/2}$  scaling.

#### 4.4.2. Subcriticality and vortex-stretching in 3D

In this section, using a 3D version of our code to integrate the NLSE, we study 3D instabilities of the basic 2D superflow.

*Preparation method:* We used the 2D laminar stationary solution  $\psi_{0V}(x, y)$  (corresponding to branch (a) of the preceding section) and the one-vortex unstable stationary solution  $\psi_{1V}(x, y)$  (branch (b)) to construct the 3D initial condition

$$\psi_{3D}(x, y, z) = f_1(z)\psi_{1V}(x, y) + [1 - f_1(z)]\psi_{0V}(x, y). \tag{67}$$

The function  $f_1(z)$ , defined by

$$f_1(z) = (\tanh[(z - z_1)/\Delta_z] - \tanh[(z - z_2)/\Delta_z])/2,$$

takes the value 1 for  $z_1 \leq z \leq z_2$  and 0 elsewhere, with  $\Delta_z$  an adaptation length.

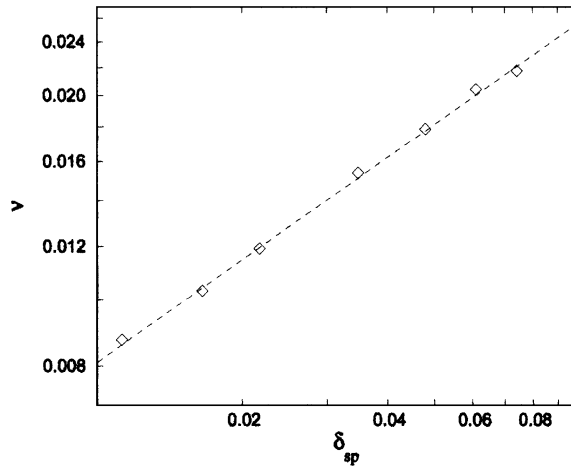


Fig. 14. Vortex emission frequency as a function of  $\delta_{sp} = (M - M^c)/M^c \ll 1$  (with  $M^c = 0.3817$ ), for a symmetric wake and  $\xi/D = \frac{1}{20}$ . The dashed line shows a fit of a polynomial  $\nu = K_1 \delta_{sp}^{1/2}$  with  $K_1 = 0.081$ . The obtained  $\delta_{sp}^{1/2}$  law for the frequency is equivalent to that expected for a dissipative system.

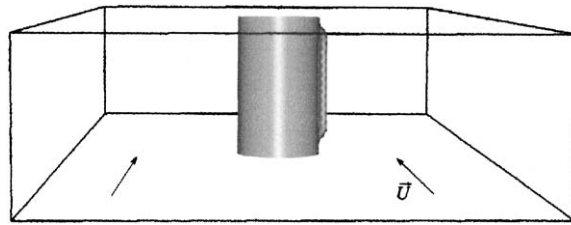


Fig. 15. Initial condition of a vortex pinned to the cylinder generated by Eq. (67). The surface  $|\psi_{BD}| = 0.5$  is shown for  $\xi/D = 0.025$ ,  $|U|/c = 0.26$  and  $\Delta_z = 2\sqrt{2}\xi$  in the  $[L_x \times L_y \times L_z]$  periodicity box ( $L_x/D = 2.4\sqrt{2}\pi$ ,  $L_y/D = 1.2\sqrt{2}\pi$  and  $L_z/D = 0.4\sqrt{2}\pi$ ).

Fig. 15 represents a 3D initial data prepared with this method for  $\xi/D = 0.025$ ,  $|U|/c = 0.26$  and  $\Delta_z = 2\sqrt{2}\xi$  in the  $[L_x \times L_y \times L_z]$  periodicity box ( $L_x/D = 2.4\sqrt{2}\pi$ ,  $L_y/D = 1.2\sqrt{2}\pi$  and  $L_z/D = 0.4\sqrt{2}\pi$ ). The surface  $|\psi_{BD}| = 0.5$  defines the cylindrical surface and the initial condition vortex line, with both ends pinned to the right side of the cylinder.

*Short-time dynamics:* Starting from the initial condition (67), the evolution of the NLSE time integration shows different short- and long-time dynamics.

During the short-time dynamics, the initial pinned vortex line rapidly contracts, evolving through a decreasing number of half-ring-like loops, down to a single quasi-stationary half-ring (see Figs. 16a–c). This evolution takes place mainly on the plane perpendicular to the flow, provided that the initial vortex is long enough to contract to a quasi-stationary half-ring as shown in Fig. 16c. Otherwise, the vortex line collapses against the cylinder while moving upstream.

Note that this quasi-stationary half-ring has been used by Varoquaux (Ihas et al., 1992; Avenel et al., 1993) to estimate the nucleation barrier in a 3D experiment.

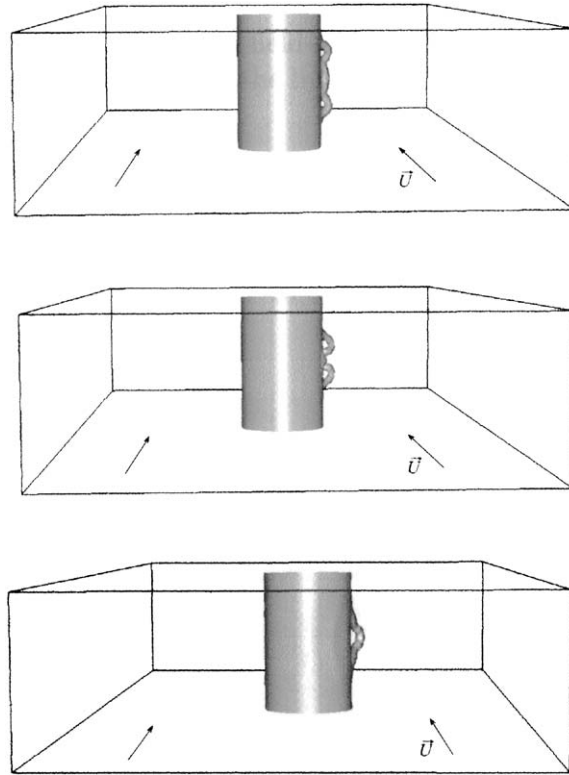


Fig. 16. Short-time dynamics for  $\xi/D = \frac{1}{40}$  and  $|\mathbf{U}|/c = 0.25$  starting from Fig. 15: A ( $t = 5\xi/c$ ), B ( $t = 10\xi/c$ ) and C ( $t = 15\xi/c$ ). The contraction of the initial vortex line occurs in the plane perpendicular to the flow. The half-rings have a diameter compatible with that of a quasi-stationary half-ring (see text).

The dynamics of the half-ring situation (Fig. 16c) is very slow and can be shown to be close to a stationary field. Indeed, the local flow velocity  $v$  in an Eulerian flow around a cylindrical obstacle is known to vary from  $v = |\mathbf{U}|$  at infinity to  $v = 2|\mathbf{U}|$  at both sides of its surface. Moreover, the diameter  $d$  of a stationary vortex ring in an infinite Eulerian flow with no obstacle is given by (Donnelly, 1991):

$$|\mathbf{U}|/c = (\sqrt{2}\xi/d)[\ln(4d/\xi) - K], \quad (68)$$

where  $|\mathbf{U}|$  is the flow velocity at infinity and the vortex core model constant  $K \sim 1$  is obtained by fitting the numerical results in Jones and Roberts (1982). Therefore, for the values used in Figs. 16, we expect that local velocities range from  $v = 0.25$  to  $v = 2 \times 0.25$ . Eq. (68) thus implies that the diameter of an hypothetical stationary half-ring should be bounded by  $d(v = |\mathbf{U}| = 0.25) = 18.8\xi$  and  $d(v = 2|\mathbf{U}| = 0.5) = 6.3\xi$ . The diameter  $d \approx 9\xi$  measured on the half-ring observed in Fig. 16c is consistent with its quasi-stationary behavior. Similarly the diameter of the half-ring shown on Fig. 18,  $d \approx 7.6\xi$ , is also found to be between the corresponding bounds  $d(0.35) = 11.4\xi$  and  $d(2 \times 0.35) = 3\xi$ .

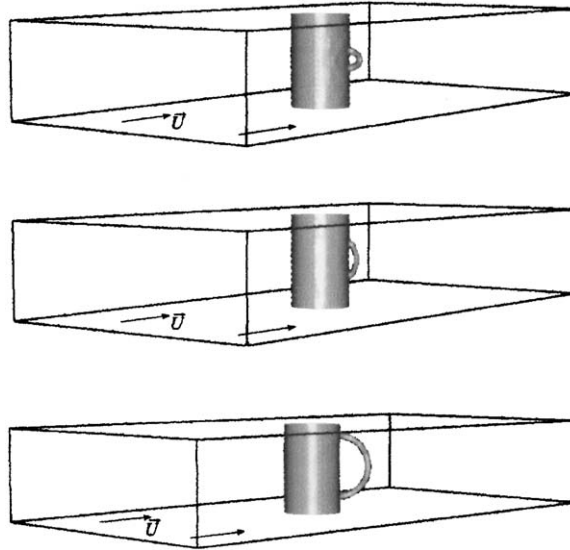


Fig. 17. Long-time dynamics for  $\xi/D = \frac{1}{40}$  and  $|\mathbf{U}|/c = 0.25$  starting from Fig. 16c. The half-ring moves downstream while growing.

*Vortex stretching as a subcritical drag mechanism:* A small perturbation over the half-ring solution can drive the system into two opposite situations where the half-ring either starts moving upstream or downstream.

When driven upstream, the half-ring eventually collapses against the cylinder, dissipating its energy as sound waves. Otherwise, the vortex loop is stretched while the pinning points move towards the back of the cylinder. Fig. 17 show the long-time dynamics for a stretching case with  $\xi/D = \frac{1}{40}$  and  $|\mathbf{U}|/c = 0.25$  starting from Fig. 16c. Fig. 19 shows a later situation for  $\xi/D = \frac{1}{20}$  and  $|\mathbf{U}|/c = 0.35$  starting from Fig. 18. As the vortex loop grows, its backmost part remains oblique to the flow. This vortex stretching mechanism consumes energy, thus generating drag. It could be responsible for the appearance of drag in experimental superflows if fluctuations are strong enough to nucleate the initial vortex loop (which is imposed extrinsically in our numerical system). Note that it takes place for 2D subcritical velocities.

Fig. 20 displays several numerical and experimental (Wilks, 1967) critical Mach numbers ( $V_c/C$ ) with respect to  $D/\xi$ , which seem to follow a  $(-1)$  slope in a log–log plot. The squares stand for our numerical stretching cases while the crosses correspond to nonstretching cases. There is a frontier between the 3D numerical dissipative and nondissipative cases (Nore et al., 2000). For  $\frac{1}{30} < \xi/D < \frac{1}{20}$ , the frontier corresponds to the expression  $R_s = 5.5$  with

$$R_s \equiv |\mathbf{U}|D/c\xi = MD/\xi. \quad (69)$$

This superfluid ‘Reynolds’ number is defined in the same way as the standard (viscous) Reynolds number  $Re \equiv |\mathbf{U}|D/\nu$  (with  $\nu$  the kinematic viscosity). It has been shown, in the superfluid turbulent ( $R_s \gg 1$ ) regime, that  $R_s$  is equivalent to the standard (viscous) Reynolds number  $Re$  (Nore et al.,

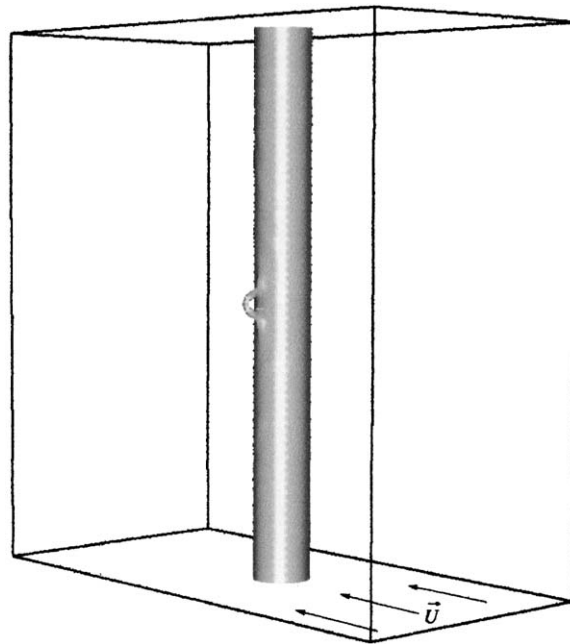


Fig. 18. Quasi-nucleation solution for  $|\mathbf{U}|/c = 0.35$  and  $\xi/D = \frac{1}{20}$  at time  $t = 15\xi/c$ .

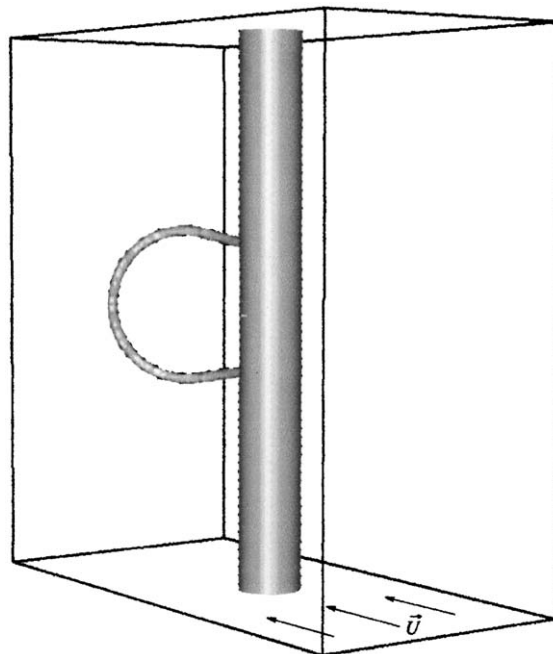


Fig. 19. Vortex stretching at  $t = 150\xi/c$  with  $|\mathbf{U}|/c = 0.35$  and  $\xi/D = 1/20$ . The vortex line is oblique to the flow.

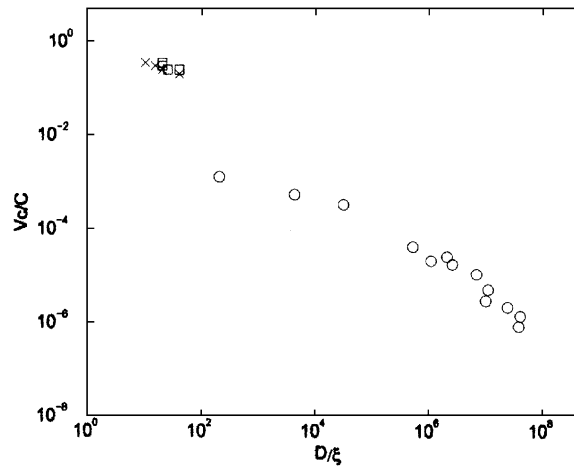


Fig. 20. Critical Mach number  $V_c/C$  versus scale ratio of numerical and experimental data  $D/\xi$ . Circles correspond to several experiments from Wilks (1967). Squares stand for our numerical stretching cases while crosses correspond to nonstretching cases (Nore et al., 2000). Note the wide difference in values of parameter  $\xi/D \simeq 10^{-1}$  for our numerics (corresponding to current experiments in BEC) and  $\xi/D$  down to  $10^{-8}$  older experiments in liquid Helium).

1997a, b; Abid et al., 1998). Note that, for a Bose condensate of particles of mass  $m$ , the quantum of velocity circulation around a vortex,  $\Gamma = 2\pi\sqrt{2}c\xi$ , has the Onsager–Feynman value  $\Gamma = h/m$  ( $h$  is Planck’s constant) and the same physical dimensions  $L^2T^{-1}$  as  $v$ .

The value of  $R_s$  divides the space of parameters into a laminar flow zone and a recirculating flow zone, very much like in the problem of a circular disc in a viscous fluid in which this frontier is also found to be around  $Re \sim 5$ . Thus, there seems to exist some degree of universality between viscous normal fluids and superfluids modeled by NLSE as discussed in Nore et al. (1997a, b) and Abid et al. (1998). In the context of superfluid  $^4\text{He}$  flow, the experimental critical velocity is known to depend strongly on the system’s characteristic size  $D$ . It is often found to be well below the Landau value (based on the velocity of roton excitation) except for experiments in which ions are dragged in liquid helium. Feynman’s alternative critical velocity criterion  $R_s \sim \log(D/\xi)$  is based on the energy needed to form vortex lines. It produces better estimates for various experimental settings, but does not describe the vortex nucleation mechanism (Donnelly, 1991).

In a recent experiment, Raman et al. have studied dissipation in a Bose–Einstein condensed gas by moving a blue detuned laser beam through the condensate at different velocities (Raman et al., 1999). In their inhomogeneous condensate, they observed a critical Mach number for the onset of 1.6 times smaller than the 2D critical Mach number  $M_{2D}^c$ .

Our computations were performed for values of  $\xi/D$  comparable to those in Bose–Einstein condensed gas experiments. They demonstrate the possibility of a subcritical drag mechanism, based on 3D vortex stretching. It would be very interesting to determine experimentally the dependence of the critical Mach number on the parameter  $\xi/D$  and the nature (2D or 3D) of the excitations (Nore et al., 2000).

#### 4.5. Stability of attractive Bose–Einstein condensates

In this section, following reference (Huepe et al., 1999, 2003), we study condensates with attractive interactions which are known to be metastable in spatially localized systems, provided that the number of condensed particles is below a critical value  $\mathcal{N}_c$  (Bradley et al., 1997). Various physical processes compete to determine the lifetime of attractive condensates. Among them one can distinguish macroscopic quantum tunneling (MQT) (Stoof, 1997; Ueda and Leggett, 1998), inelastic two and three body collisions (ICO) (Dodd et al., 1996; Shi and Zheng, 1997) and thermally induced collapse (TIC) (Stoof, 1997; Sackett et al., 1998). We compute the life-times, using both a variational Gaussian approximation and the exact numerical solution for the condensate wave-function.

##### 4.5.1. Computations of stationary states

*Gaussian approximation:* A Gaussian approximation for the condensate density can be obtained analytically through the following procedure.

Inserting

$$\psi(r, \tilde{t}) = A(\tilde{t}) \exp(-r^2/2r_G^2(\tilde{t}) + ib(\tilde{t})r^2) \quad (70)$$

into action (45), where  $\mathcal{F}$  is given by (52), yields a set of Euler–Lagrange equations for  $r_G(\tilde{t})$ ,  $b(\tilde{t})$  and the (complex) amplitude  $A(\tilde{t})$ . The stationary solutions of the Euler–Lagrange equations produce the following values (Huepe et al., 1999):

$$\mathcal{N}(\mu) = \frac{4\sqrt{2\pi^3}(-8\mu + 3\sqrt{7 + 4\mu^2})}{7|\tilde{a}|(-2\mu + \sqrt{7 + 4\mu^2})^{3/2}}, \quad (71)$$

$$\mathcal{E} = \mathcal{N}(\mu)(-\mu + 3\sqrt{7 + 4\mu^2})/7. \quad (72)$$

$\mathcal{N}$  is found to be maximal at  $\mathcal{N}_c^G = 8\sqrt{2\pi^3}/|5^{5/4}\tilde{a}|$ . The corresponding value of the chemical potential is  $\mu = \mu_c^G = \frac{1}{2}\sqrt{5}$ .

Linearizing the Euler–Lagrange equations around the stationary solutions, we obtain the following expression for the eigenvalues (Huepe et al., 1999):

$$\lambda^2(\mu) = 8\mu^2 - 4\mu\sqrt{7 + 4\mu^2} + 2. \quad (73)$$

This qualitative behavior is the generic signature of a Hamiltonian saddle-node (HSN) bifurcation defined, at lowest order, by the normal form (Guckenheimer and Holmes, 1983)

$$m_{\text{eff}}\ddot{Q} = \delta - \beta Q^2, \quad (74)$$

where  $\delta = (1 - \mathcal{N}/\mathcal{N}_c)$  is the bifurcation parameter. The critical amplitude  $Q$  is related to the radius of the condensate (Huepe et al., 1999). We can relate the parameters  $\beta$  and  $m_{\text{eff}}$  to critical scaling laws, by defining the appropriate energy

$$\mathcal{E} = \mathcal{E}_0 + m_{\text{eff}}\dot{Q}^2/2 - \delta Q + \beta Q^3/3 - \gamma\delta. \quad (75)$$

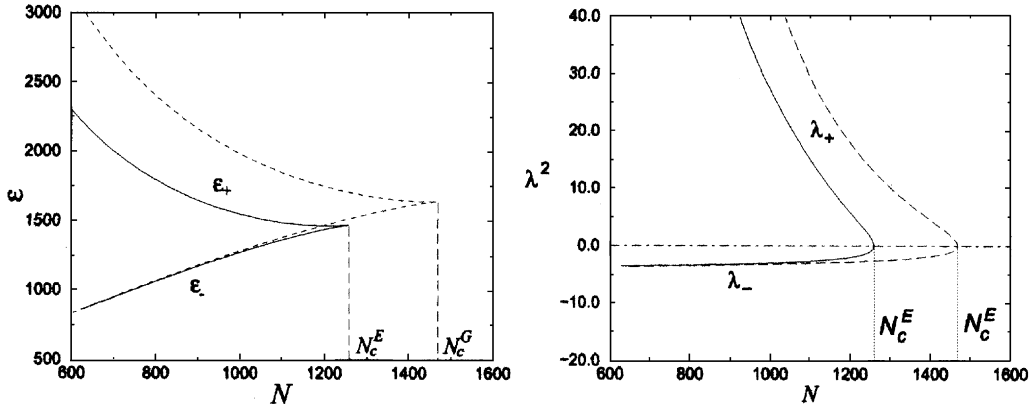


Fig. 21. Stationary solutions of the NLSE versus particle number  $\mathcal{N}$ . Left: value of the energy functional  $\mathcal{E}_-$  on the stable (elliptic) branch and  $\mathcal{E}_+$  on the unstable (hyperbolic) branch. Right: square of the bifurcating eigenvalue ( $\lambda_{\pm}^2$ );  $|\lambda_-|$  is the frequency of small excitations around the stable branch. Solid lines: exact solution of the NLSE. Dashed lines: Gaussian approximation.

From (74) it is straightforward to derive, close to the critical point  $\delta = 0$ , the universal scaling laws

$$\mathcal{E}_{\pm} = \mathcal{E}_c - \mathcal{E}_l \delta \pm \mathcal{E}_A \delta^{3/2}, \tag{76}$$

$$\lambda_{\pm}^2 = \pm \lambda_A^2 \delta^{1/2}, \tag{77}$$

where  $\mathcal{E}_c = \mathcal{E}_0$ ,  $\mathcal{E}_l = \gamma$ ,  $\mathcal{E}_A = \frac{2}{3} \sqrt{\beta}$  and  $\lambda_A^2 = 2\sqrt{\beta}/m_{\text{eff}}$ .

*Numerical branch following:* Using the branch-following method described in Section 4.3, we have computed the exact stationary solutions of the NLSE. We use the following value  $\tilde{a} = -5.74 \times 10^{-3}$ , that corresponds to experiments with  ${}^7\text{Li}$  atoms in a radial trap (Bradley et al., 1995, 1997).

As is apparent in Fig. 21, the exact critical value  $\mathcal{N}_c^E = 1258.5$  is smaller than the Gaussian value  $\mathcal{N}_c^G = 1467.7$  (Ruprecht et al., 1995; Ueda and Leggett, 1998). The critical amplitudes corresponding to the Gaussian approximation can be computed from (71) and (72). One finds  $\mathcal{E}_c = 4\sqrt{2\pi^3}/|5^{3/4}\tilde{a}|$ ,  $\mathcal{E}_A = 64\sqrt{\pi^3}/|5^{9/4}\tilde{a}|$  and  $\lambda_A^2 = 4\sqrt{10}$ . For the exact solutions, we obtain the critical amplitudes by performing fits on the data. One finds  $\mathcal{E}_A = 1340$  and  $\lambda_A^2 = 14.68$ . Thus, the Gaussian approximation captures the bifurcation qualitatively, but with quantitative 17% error on  $\mathcal{N}_c$  (Ruprecht et al., 1995), 24% error on  $\mathcal{E}_A$  and 14% error on  $\lambda_A^2$ . Fig. 22 shows the physical origin of the quantitative errors in the Gaussian approximation. By inspection it is apparent that the exact solution is well approximated by a Gaussian only for small  $\mathcal{N}$  on the stable (elliptic) branch.

#### 4.5.2. Estimation of life-times

In this section, we estimate the decay rates due to thermally induced collapse, macroscopic quantum tunneling and inelastic collisions.

*Thermally induced collapse:* The thermally induced collapse (TIC) rate  $\Gamma_T$  is estimated using the formula (Gardiner, 1985)

$$\frac{\Gamma_T}{\omega} = \frac{|\lambda_+|}{2\pi} \exp \left[ \frac{-\hbar\omega(\mathcal{E}_+ - \mathcal{E}_-)}{k_B T} \right], \tag{78}$$

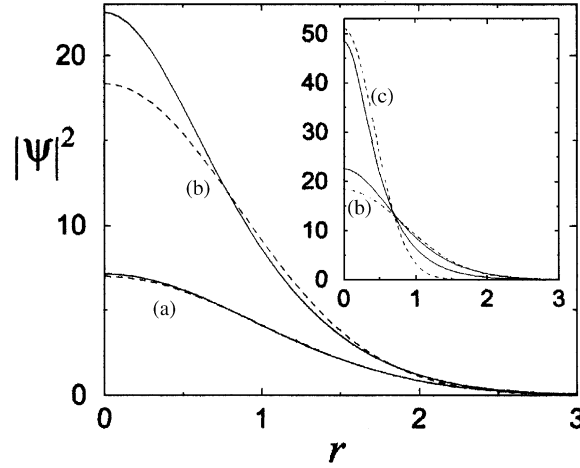


Fig. 22. Condensate density  $|\psi|^2$  versus radius  $r$ , in reduced units (see text). Solid lines: exact solution of the NLSE. Dashed lines: Gaussian approximation. Stable (elliptic) solutions are shown for particle number  $\mathcal{N}=252$  (a) and  $\mathcal{N}=1132$  (b). (c) is the unstable (hyperbolic) solution for  $\mathcal{N}=1132$  (see insert).

where  $\hbar\omega(\mathcal{E}_+ - \mathcal{E}_-)$  is the (dimensionalized) height of the nucleation energy barrier,  $T$  is the temperature of the condensate and  $k_B$  is the Boltzmann constant. Note that the prefactor characterizes the typical decay time which is controlled by the slowest part of the nucleation dynamics: the top-of-the-barrier saddle point eigenvalue  $\lambda_+$ . The behavior of  $\Gamma_T$  can be obtained directly from the universal saddle-node scaling laws (76) and (77). Thus the exponential factor and the prefactor vanish, respectively, as  $\delta^{3/2}$  and  $\delta^{1/4}$ .

*Macroscopic quantum tunneling:* We estimate the MQT decay rate using an instanton technique that takes into account the semi classical trajectory giving the dominant contribution to the quantum action path integral (Stoof, 1997; Ueda and Leggett, 1998). This trajectory is approximated as the solution of

$$\frac{d^2q(t)}{dt^2} = -\frac{d\tilde{\Phi}(q)}{dq}. \quad (79)$$

$\tilde{\Phi}(q)$  is a polynomial such that  $-\tilde{\Phi}(q)$  reconstructs the Hamiltonian dynamics, and is determined by the relations

$$\tilde{\Phi}(q_m) = -\mathcal{E}_+, \quad (80)$$

$$\tilde{\Phi}(q_f) = -\mathcal{E}_-, \quad (81)$$

$$\partial_q^2 \tilde{\Phi}(q_m) = |\lambda_+(\mathcal{N})|, \quad (82)$$

$$\partial_q^2 \tilde{\Phi}(q_f) = -|\lambda_-(\mathcal{N})|. \quad (83)$$

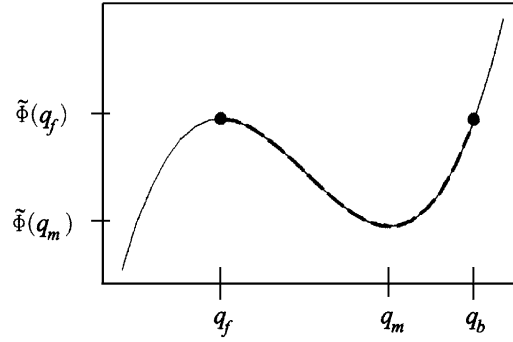


Fig. 23. The bounce trajectory is shown as dashes, above the potential  $\tilde{\Phi}(q)$ .

The bounce trajectory is displayed in Fig. 23 (dashed line) above the potential  $\tilde{\Phi}(q)$ . The MQT rate is estimated as

$$\frac{\Gamma_Q}{\omega} = \sqrt{\frac{|\lambda_-|v_0^2}{4\pi}} \exp \left[ \frac{-4}{\sqrt{2}} \int_{q_f}^{q_b} \sqrt{\tilde{\Phi}(q) - \tilde{\Phi}(q_f)} dq \right], \quad (84)$$

where  $v_0$  is defined by the asymptotic form of the bounce trajectory  $q(t)$  (Stoof, 1997):  $q(\tau) \sim q_f + (v_0/|\lambda_-|) \exp[-|\lambda_- \tau|]$ . Universal scaling laws can be derived close to criticality from (74), (76) and (77). The exponential factor in (84) follows the same scaling than  $\sqrt{|\mathcal{E}_+ - \mathcal{E}_-|} dq$ . It therefore vanishes as  $\delta^{5/4}$ . From the asymptotic form of  $q(t)$ ,  $dq$  follows the same law as  $v_0/|\lambda_-|$ . Thus  $v_0 \sim \delta^{3/4}$  and the prefactor vanishes as  $\delta^{7/8}$ .

*Inelastic collision:* The inelastic collision rate (ICO) is estimated using the relation

$$\frac{d\mathcal{N}}{dt} = f_C(\mathcal{N}) \quad (85)$$

with

$$f_C(\mathcal{N}) = K \int |\psi|^4 d^3\tilde{\mathbf{x}} + L \int |\psi|^6 d^3\tilde{\mathbf{x}}, \quad (86)$$

where  $K = 3.8 \times 10^{-4}$  and  $L = 2.6 \times 10^{-7} \text{ s}^{-1}$ . The ICO rate can be evaluated from the stable branch alone. In order to compare the particle decay rate  $f_C(\mathcal{N})$  to the condensate collective decay rates obtained for TIC and MQT, we compute the condensate ICO half-life as

$$\tau_{1/2}(\mathcal{N}) = \int_{\mathcal{N}/2}^{\mathcal{N}} dn / f_C(n) \quad (87)$$

and plot  $\tau_{1/2}^{-1}$  in Fig. 24.

*Discussion:* It is apparent by inspection of Fig. 24 that for a given value of  $\mathcal{N}$  the exact and Gaussian approximate rates are dramatically different. We now compare the relative importance of the different exact decay rates. At  $T \leq 1 \text{ nK}$ , the MQT effect becomes important compared to the ICO decay in a region very close to  $\mathcal{N}_c^E$  ( $\delta \leq 8 \times 10^{-3}$ ) as was shown in Ueda and Leggett (1998) using Gaussian computations but evaluating them with the exact maximal number of condensed particles  $\mathcal{N}_c^E$ . Considering thermal fluctuations for temperatures as low as 2 nK, it is apparent in Fig. 24 (see

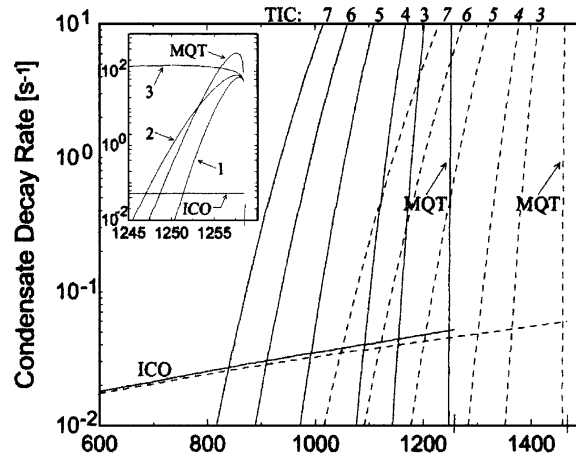


Fig. 24. Condensate decay rates versus particle number. ICO: inelastic collisions. MQT: macroscopic quantum tunneling. TIC: thermally induced collapse at temperatures 1 nK (1), 2 nK (2), 50 nK (3), 100 nK (4), 200 nK (5), 300 nK (6) and 400 nK (7). The insert shows the details of the cross-over region between quantum tunneling and thermal decay rate. Solid lines: exact solution of the NLSE, dashed lines: Gaussian approximation.

insert) that the MQT will be the dominant decay mechanism only in a region extremely close to  $\mathcal{N}_c$  ( $\delta < 5 \times 10^{-3}$ ) where the condensates will live less than  $10^{-1}$  s. Thus, in the experimental case of  $^7\text{Li}$  atoms, the relevant effects are ICO and TIC, with cross-over determined in Fig. 24.

Calculations similar to those described here have also been generalized to an attractive Bose–Einstein condensate confined by a cylindrically symmetric potential  $V(r) = m(\omega_r^2 r^2 + \omega_z^2 z^2)/2$ , which lead to cigar-shaped or pancake-shaped condensates. Newton’s method was used to calculate stationary states, as described above. The inverse Arnoldi method was used to calculate the leading eigenvalues  $\lambda_{\pm}^2$ , yielding decay rates that are similar to those computed for the spherically symmetric case. This was found to be due to spontaneous isotropization of the condensates. See Huepe et al. (2003) for more details.

## 5. Conclusion

The main result of the NLSE simulations presented in Section 3.2 is that two diagnostics of Kolmogorov’s regime in decaying turbulence are satisfied. These diagnostics are, at the time of the maximum of energy dissipation: (i) a parameter-independent kinetic energy dissipation rate and (ii) a  $k^{-5/3}$  spectral scaling in the inertial range. Thus, the NLSE simulations were shown to be very similar, as far as the energy cascade is concerned, with the viscous simulations. The experimental results presented in Section 3.3 prove that the Kolmogorov cascade survives in the superfluid regime.

We have seen that the numerical tools developed in Section 4.3 can be used in practice to obtain the stationary solutions of the NLSE. These methods have allowed us to find the full bifurcation diagrams of Bose–Einstein condensates with attractive interactions and superflows past a cylinder. Furthermore, the stationary solutions have given us efficient way to start vortical dynamics (in 2D and 3D) in a controlled manner.

## Acknowledgements

The work reviewed in this paper was performed in collaboration with G. Dewel, J. Maurer and P. Tabeling. It was supported by ECOS-CONICYT program no. C01E08 and by the NSF DMR 0094569. Computations were performed at the Institut du Développement et des Ressources en Informatique Scientifique.

## References

- Abid, M., Brachet, M., Maurer, J., Nore, C., Tabeling, P., 1998. Experimental and numerical investigations of low-temperature superfluid turbulence. *Eur. J. Mech. B Fluids* 17 (4), 665–675.
- Anderson, M.H., Ensher, J.R., Matthews, M.R., Wieman, C.E., Cornell, E.A., 1995. Observation of Bose–Einstein condensation in a dilute atomic vapor. *Science* 269, 198.
- Araki, T., Tsubota, M., 2000. Cascade process of vortex tangle dynamics in superfluid  $^4\text{He}$  without mutual friction. *J. Low Temp. Phys.* 121, 405.
- Araki, T., Tsubota, M., Nemirovskii, S.K., 2002. Energy spectrum of superfluid turbulence with no normal-fluid component. *Phys. Rev. Lett.* 89 (14), 1–4.
- Avenel, O., Ihas, G.G., Varoquaux, E., 1993. The nucleation of vortices in superfluid  $^4\text{He}$ : answers and questions. *J. Low Temp. Phys.* 93, 1031–1057.
- Barenghi, C.F., Donnelly, R.J., Vinen, W.F. (Eds.), 2001. *Quantized Vortex Dynamics and Superfluid Turbulence*, Lecture Notes in Physics.
- Brachet, M., 1990. Géométrie des structures à petite échelle dans le vortex de Taylor–Green. *C.R. Acad. Sci.* 311, 775.
- Brachet, M.E., Meiron, D.I., Orszag, S.A., Nickel, B.G., Morf, R.H., Frisch, U., 1983. Small-scale structure of the Taylor–Green vortex. *J. Fluid Mech.* 130, 411–452.
- Bradley, C.C., Sackett, C.A., Tollett, J.J., Hulet, R.G., 1995. Evidence of Bose–Einstein condensation in an atomic gas with attractive interactions. *Phys. Rev. Lett.* 75 (9), 1687.
- Bradley, C.C., Sackett, C.A., Hulet, R.G., 1997. Bose–Einstein condensation of lithium: observation of limited condensate number. *Phys. Rev. Lett.* 78 (6), 985.
- Bretin, V., Rosenbush, P., Chevy, F., Shlyapnikov, G.V., Dalibard, J., 2003. Quadrupole oscillation of a single-vortex condensate: evidence for Kelvin modes. *Phys. Rev. Lett.* 90, 100403.
- Dalfovo, F., Giorgini, S., Pitaevskii, L.P., Stringari, S., 1999. Theory of Bose–Einstein condensation in trapped gases. *Rev. Mod. Phys.* 71 (3).
- Davis, K.B., Mewes, M.O., Andrews, M.R., van Druten, N.J., Durfee, D.S., Kurn, D.M., Ketterle, W., 1995. Bose–Einstein condensation in a gas of sodium atoms. *Phys. Rev. Lett.* 75, 3969.
- Davis, S.I., Hendry, P.C., McClintock, P.V.E., 2000. Decay of quantized vorticity in superfluid  $^4\text{He}$  at mK temperature. *Physica B* 280, 43–44.
- Dodd, R.J., Edwards, M., Williams, C.J., Clark, C.W., Holland, M.J., Ruprecht, P.A., Burnett, K., 1996. Role of attractive interactions on Bose–Einstein condensation. *Phys. Rev. A* 54 (1), 661.
- Domaradzki, J., Liu, W., Brachet, M., 1993. An analysis of subgrid-scale interactions in numerically simulated isotropic turbulence. *Phys. Fluids A* 5, 1747.
- Donnelly, R.J., 1991. *Quantized Vortices in Helium II*. Cambridge University Press, Cambridge.
- Douady, S., Couder, Y., Brachet, M.E., 1991. Direct observation of the intermittency of intense vorticity filaments in turbulence. *Phys. Rev. Lett.* 67, 983.
- Fauve, S., Laroche, C., Castaing, B., 1993. Pressure fluctuations in swirling turbulent flows. *J. Phys. II* 3, 271.
- Frisch, U., 1995. *Turbulence, the Legacy of A.N. Kolmogorov*. Cambridge University Press, Cambridge.
- Frisch, T., Pomeau, Y., Rica, S., 1992. Transition to dissipation in a model of superflow. *Phys. Rev. Lett.* 69, 1644.
- Gardiner, C.W., 1985. *Handbook of Stochastic Methods*. Springer, Berlin.
- Gottlieb, D., Orszag, S.A., 1977. *Numerical Analysis of Spectral Methods*. SIAM, Philadelphia.
- Gross, E.P., 1961. Structure of a quantized vortex in boson systems. *Nuovo Cimento* 20 (3) 454.

- Guckenheimer, J., Holmes, P., 1983. *Nonlinear Oscillations, Dynamical Systems and Bifurcations of Vector Fields*. Springer, Berlin.
- Hakim, V., 1997. Nonlinear Schrödinger flow past an obstacle in one dimension. *Phys. Rev. E* 55 (3), 2835–2845.
- Huepe, C., Brachet, M.-E., 1997. Solutions de nucléation tourbillonnaires dans un modèle d'écoulement superfluide. *C.R. Acad. Sci. Paris* 325 (II), 195–202.
- Huepe, C., Brachet, M.E., 2000. Scaling laws for vortical nucleation solutions in a model of superflow. *Physica D* 140, 126–140.
- Huepe, C., Métens, S., Dewel, G., Borckmans, P., Brachet, M.-E., 1999. Decay rates in attractive Bose–Einstein condensates. *Phys. Rev. Lett.* 82 (2), 1616.
- Huepe, C., Tuckerman, L.S., Métens, S., Brachet, M.-E., 2003. Stability and decay rates of non-isotropic attractive Bose–Einstein condensates. *Phys. Rev. A* 68, 023609.
- Ihas, G.G., Avenel, O., Aarts, R., Salmelin, R., Varoquaux, E., 1992. Quantum nucleation of vortices in the flow of superfluid He-4 through an orifice. *Phys. Rev. Lett.* 69 (2), 327.
- Inouye, S., Gupta, S., Rosenband, T., Chikkatur, A.P., Görlitz, A., Gustavson, T.L., Leanhardt, A.E., Pritchard, D.E., Ketterle, W., 2001. Observation of vortex phase singularities in Bose–Einstein condensates. *Phys. Rev. Lett.* 87, 080402.
- Jones, C.A., Roberts, P.H., 1982. Motions in a Bose condensate: IV. axisymmetric solitary waves. *J. Phys. A* 15, 2599.
- Kawatra, M.P., Pathria, R.K., 1966. Quantized vortices in imperfect Bose gas. *Phys. Rev.* 151, 1.
- Kivotides, D., Vassilicos, J.C., Samuels, D.C., Barenghi, C.F., 2001. Kelvin waves cascade in superfluid turbulence. *Phys. Rev. Lett.* 86, 3080–3083.
- Klein, R., Majda, A.J., 1991. Self-stretching of perturbed vortex filaments. *Physica D* 53, 267.
- Koplik, J., Levine, H., 1993. Vortex reconnection in superfluid Helium. *Phys. Rev. Lett.* 71, 1375–1378.
- Landau, L., Lifchitz, E., 1980. *Fluid Mechanics*. Pergamon Press, Oxford.
- Leadbeater, M., Samuels, D.C., Barenghi, C.F., Adams, C.S., 2003. Decay of superfluid turbulence via Kelvin-wave radiation. *Phys. Rev. A* 67, 015601.
- Lund, F., 1991. Defect dynamics for the nonlinear Schrödinger equation derived from a variational principle. *Phys. Rev. Lett.* A 159, 245.
- Madison, K.W., Chevy, F., Wohlleben, W., Dalibard, J., 2000. Vortex formation in a stirred Bose–Einstein condensate. *Phys. Rev. Lett.* 84, 806–809.
- Mamun, C., Tuckerman, L., 1995. Asymmetry and Hopf bifurcation in spherical Couette flow. *Phys. Fluids* 7 (1), 80.
- Matthews, M.R., Anderson, B.P., Haljan, P.C., Hall, D.S., Wieman, C.E., Cornell, E.A., 1999. Vortices in a Bose–Einstein condensate. *Phys. Rev. Lett.* 83, 2498–2501.
- Maurer, J., Tabeling, P., 1998. Local investigation of superfluid turbulence. *Europhys. Lett.* 43 (1), 29–34.
- Neu, J.C., 1990. Vortices in complex scalar fields. *Physica D* 43, 385.
- Nore, C., Brachet, M., Fauve, S., 1993. Numerical study of hydrodynamics using the nonlinear Schrödinger equation. *Physica D* 65, 154–162.
- Nore, C., Abid, M., Brachet, M., 1994. Simulation numérique d'écoulements cisailés tridimensionnels à l'aide de l'équation de Schrödinger non linéaire. *C.R. Acad. Sci.* 319 II (7), 733.
- Nore, C., Abid, M., Brachet, M., 1997a. Decaying Kolmogorov turbulence in a model of superflow. *Phys. Fluids* 9 (9), 2644.
- Nore, C., Abid, M., Brachet, M.E., 1997b. Kolmogorov turbulence in low-temperature superflows. *Phys. Rev. Lett.* 78 (20), 3896–3899.
- Nore, C., Huepe, C., Brachet, M.E., 2000. Subcritical dissipation in three-dimensional superflows. *Phys. Rev. Lett.* 84 (10), 2191.
- Nozières, P., Pines, D., 1990. *The Theory of Quantum Liquids*. Addison-Wesley, New York.
- Ogawa, S.I., Tsubota, M., Hattori, Y., 2002. Study of reconnection and acoustic emission of quantized vortices in superfluid by the numerical analysis of the Gross–Pitaevskii equation. *J. Phys. Soc. Japan* 71, 813.
- Pham, C.-T., Brachet, M., 2002. Dynamical scaling laws in two types of extended Hamiltonian systems at dissipation onset. *Physica D* 163, 129–147.
- Pitaevskii, L.P., 1961. Vortex lines in an imperfect Bose gas. *Sov. Phys.-JETP* 13 (2), 451.
- Pomeau, Y., Rica, S., 1993. Model of superflow with rotons. *Phys. Rev. Lett.* 71 (2), 247.
- Press, W., Teukolsky, S., Vetterling, W., Flannery, B., 1994. *Numerical Recipes in Fortran*. Cambridge University Press, Cambridge.

- Raman, C., Köhl, M., Onofrio, R., Durfee, D.S., Kuklewicz, C.E., Hadzibabic, Z., Ketterle, W., 1999. Evidence for a critical velocity in a Bose–Einstein condensed gas. *Phys. Rev. Lett.* 83 (13), 2502.
- Roberts, P.H., Berloff, N.G., 2001. The nonlinear Schrödinger equation as a model of superfluidity. In: Barenghi, C.F., Donnelly, R.J., Vinen, W.F. (Eds.), *Quantized Vortex Dynamics and Superfluid Turbulence*, Lecture Notes in Physics. Springer, Berlin, pp. 235–256.
- Rosenbush, P., Bretin, V., Dalibard, J., 2002. Dynamics of a single vortex line in a Bose–Einstein condensate. *Phys. Rev. Lett.* 89, 200403-1.
- Ruprecht, P.A., Holland, M.J., Burnett, K., Edwards, M., 1995. Time-dependent solution of the nonlinear Schrödinger equation for Bose-condensed trapped neutral atoms. *Phys. Rev. A* 51 (6), 4704.
- Sackett, C.A., Stoof, H.T.C., Hulet, R.G., 1998. Growth and collapse of a Bose–Einstein condensate with attractive interactions. *Phys. Rev. Lett.* 80 (10), 2031.
- Schwarz, K.W., 1985. Three-dimensional vortex dynamics in superfluid  $^4\text{He}$ : line–line and line–boundary interactions. *Phys. Rev. B* 31, 5782.
- Seydel, R., 1988. *From Equilibrium to Chaos: Practical Bifurcation and Stability Analysis*. Elsevier, New York.
- Shi, H., Zheng, W.-M., 1997. Bose–Einstein condensation in an atomic gas with attractive interactions. *Phys. Rev. A* 55 (4), 2930.
- Spiegel, E.A., 1980. Fluid dynamical form of the linear and nonlinear Schrödinger equations. *Physica D* 1, 236.
- Stoof, H.T.C., 1997. Macroscopic quantum tunneling of a Bose condensate. *J. Stat. Phys.* 87, 1353.
- Svistunov, B.V., 1995. Superfluid turbulence in the low-temperature limit. *Phys. Rev. B* 52, 3647.
- Taylor, G.I., Green, A.E., 1937. Mechanism of the production of small eddies from large ones. *Proc. Soc. Lond. A* 158, 499.
- Tsuzuki, T., 1971. Nonlinear waves in the Pitaevskii–Gross equation. *J. Low Temp. Phys.* 4 (4).
- Ueda, M., Leggett, A.J., 1998. Macroscopic quantum tunneling of a Bose–Einstein condensate with attractive interaction. *Phys. Rev. Lett.* 80 (8), 1576.
- van der Vorst, H., 1992. Bi-cgstab: a fast and smoothly converging variant of bi-cg for the solution of nonsymmetric linear systems. *SIAM J. Sci. Stat. Comput.* 13, 631.
- Vinen, W.F., 2001. Decay of turbulence at a very low temperature: the radiation of sound from a Kelvin wave on a quantized vortex. *Phys. Rev. B* 64, 134520-1.
- Vinen, W.F., Niemela, J.J., 2002. Quantum turbulence. *J. Low Temp. Phys.* 128, 167–231.
- Wilks, J., 1967. *The Properties of Liquid and Solid Helium*. Clarendon Press, Oxford.
- Zakharov, V.E., Shabat, A.B., 1973. Interaction between solitons in a stable medium. *Sov. Phys.-JETP* 37 (5), 823–828.
- Zocchi, G., Tabeling, P., Maurer, J., Willaime, H., 1994. Measurement of the scaling of the dissipation at high Reynolds numbers. *Phys. Rev. E* 50, 3693.